# A High Spatiotemporal Resolution Snow Depth Inversion Solution With Multi-GNSS-IR in Complex Terrain

Rui Ding, Nanshan Zheng, Georges Stienne, Jiaxing He, Hengyi Zhang, and Xuexi Liu

***Abstract*—For high spatiotemporal resolution global navigation satellite system interferometric reflectometry (GNSS-IR) snow depth monitoring, addressing terrain effects and multi-GNSS data fusion together is essential due to their coupling. Analyzed multi-GNSS spatiotemporal availability to ensure coverage and revisit rate. Improved data usage and inversion accuracy through complete ensemble empirical mode decomposition. Corrected anisotropic terrain errors using digital elevation model to account for varied reflection footprints. A grid was established for data partitioning and fusion. Considering intersystem errors, the proposed signal peak ratio weighting (PRW) fusion of single-system inversions is based on signal quality. Then, by using inverse distance weighting, the multi-GNSS results were fused, achieving high-accuracy, hourly snow depth inversions with high spatial resolution. With terrain correction, the correlation coefficient ($R$) reached 0.984, root mean square error (RMSE) 0.136 m, and mean error (ME) –0.060 m, reduced by 9.05% and 24.84%. PRW further enhanced accuracy, increasing $R$ to 0.985, reducing RMSE 14.6% to 0.128 m, improving ME 40.57% to –0.047 m. Grid fusion effectively integrated multi-GNSS data, showing daily $R$ 0.865, RMSE 0.102 m, ME –0.050 m. Across season, $R$ 0.984, RMSE 0.134 m, ME –0.065 m. Compared to equal weighting, $R$ improved 4.72% and 3.05%, RMSE reduced 26.09% and 14.10%, ME decreased 28.57% and 16.44%. Hourly results achieved 94.44% coverage, averaging 5.19 usable tracks, demonstrating effectiveness. Overall, this article presents an end-to-end solution for high spatiotemporal resolution snow depth inversion using GNSS-IR, and the methodology can be extended to other geophysical parameter retrievals.**

***Index Terms*—Global navigation satellite system interferometric reflectometry (GNSS-IR), multi-GNSS, snow depth, terrain.**

Manuscript received 27 February 2024; revised 13 May 2024; accepted 21 July 2024. Date of publication 24 July 2024; date of current version 5 September 2024. This work was supported in part by the Joint Funds of the National Natural Science Foundation of China under Grant U22A20569, in part by the Youth Fund of the National Natural Science Foundation of China under Grant 42304015, in part by the Jiangsu Province Natural Science Foundation of China under Grant BK20231087, in part by the Open Research Fund of Key Laboratory of Land Environment and Disaster Monitoring, Ministry of Natural Resources, China University of Mining and Technology under Grant LEDM2021B11, in part by the Postgraduate Research & Practice Innovation Program of Jiangsu Province under Grant KYCX22_2586, and in part by the Graduate Innovation Program of China University of Mining and Technology under Grant 2022WLKXJ029. *(Corresponding author: Nanshan Zheng.)*

Rui Ding and Nanshan Zheng are with the Key Laboratory of Land Environment and Disaster Monitoring, Ministry of Natural Resources, China University of Mining and Technology, Xuzhou 221116, China, and also with the School of Environment Science and Spatial Informatics, China University of Mining and Technology, Xuzhou 221116, China (e-mail: ruiding@cumt.edu.cn; znshcumt@cumt.edu.cn).

Georges Stienne is with the Laboratoire d'Informatique Signal et Image de la Côte d'Opale, Université du Littoral Côte d'Opale, 62228 Calais, France (e-mail: georges.stienne@univ-littoral.fr).

Jiaxing He, Hengyi Zhang, and Xuexi Liu are with the School of Environment Science and Spatial Informatics, China University of Mining and Technology, Xuzhou 221116, China (e-mail: hjxcumt@cumt.edu.cn; ts20160195p31@cumt.edu.cn; xuexiliu@cumt.edu.cn).

Digital Object Identifier 10.1109/JSTARS.2024.3432978

## I. Introduction

SNOW is the most widely distributed component in the cryosphere, characterized by pronounced interannual and seasonal variations. It can influence local and even distant climatic changes by affecting the surface energy balance, water cycle, and atmospheric circulation patterns [1], [2], [3]. Traditional ground-based snow depth detection methods, though precise, have limited monitoring scope. While satellite-borne passive microwave methods can monitor vast snow depth variations, they are affected by saturation effects [4], [5]. In recent years, with the proliferation of satellite information, the technology of global navigation satellite system reflectometry (GNSS-R) has garnered widespread attention. This technique enables all-weather monitoring of surface parameter changes within an area of 1000 square meters surrounding existing GNSS stations [6]. The GNSS-IR method was initially used for altimetry [7]. The authors in [8], [9], [10] were the first to apply GNSS-IR technology for snow depth measurement, and experimental results indicated a consistency between the signal-to-noise ratio (SNR) frequency of the reflected signal and snow depth. Based on the forward model proposed by Nievinski et al. [11], [12], [13], many scholars began to use data from different systems and frequency bands for snow depth inversion. To enhance spatial and temporal resolution of snow depth inversion, [14] experimented with data from multiple stations in the L1 frequency band and compared the results with those from the L2C band, finding that data quality determined the inversion accuracy. Research from [15], which used L2P data from three stations for snow depth inversion, found that although the accuracy was not as good as L2C, it was robust enough to supplement L2C when data were lacking. Tabibi et al. [16] employed field measurements and simulation methods to compare the impact of different physical parameters (like reflective surface height, surface material, and surface roughness) on snow depth inversion using the L5 signal and found that there was virtually no difference between inversion results from L5 and L2 GPS signals. Qian and Jin [17] conducted snow depth inversion using SNR from GLONASS satellite's L1 and L2 frequency

bands. Experimental results were in good agreement with field-measured snow depth and showed no significant difference when compared to inversion results using GPS satellite data. Finally, Tabibi et al. [18] leveraged signals independently received from eight French GNSS stations to propose a daily snow depth time series algorithm based on a signal-specific variance factor. Compared to individual signals, this optimal statistical combination method can significantly improve the accuracy of snow depth inversion. Yu et al. [19] introduced a novel method that combined satellite data, empirical models, and existing snow measurement systems to improve the accuracy of snow depth and snow water equivalent estimations. An et al. [20] proposed an improved method for estimating snow depth by introducing wavelet decomposition before spectral analysis of GNSS observational data, and for the first time analyzed the impact of rainfall on snow depth estimation. Wang et al. [21] employed a robust regression method to combine signals from different satellite constellations for snow depth inversion. Experimental results indicate that this method can reduce uncertainties, and its accuracy is improved by up to 50% compared to single-signal methods. However, existing data fusion methods lack consideration for signal data quality and the precise location of reflection points.

Regarding the impact of errors in GNSS reflected signals on the accuracy of snow depth inversion, An et al. [20] introduced a snow depth inversion algorithm based on wavelet decomposition. Zhou et al. [22] proposed a snow depth inversion method incorporating variational mode decomposition (VMD). Li et al. [23] presented a snow depth inversion algorithm combining nonlinear least squares fitter with fast Fourier transform. Yet, existing research neglects the effects of the surrounding environment and topography of GNSS stations, and such oversight can cause significant loss in inversion accuracy and data utilization rates. Boniface et al. [24] compared the gridded snow estimates from the snow data assimilation system with the snow depth inversion values from GPS-IR at approximately 100 plate boundary observation stations in the western US. It was found that these two different datasets produced significantly different results. The analysis identified distance from the measurement point, topographic variations, and differences in vegetation as reasons for the discrepancies. Vey et al. [25] studied the impact of wind on snow depth and conducted experiments, with results indicating that the GNSS-R technology's inversion of snow depth is minimally affected by wind, which can be considered negligible. Zhang et al. [26] proposed a grid method model to correct the impact of topographic variations on snow depth inversion. Zhang et al. [27] introduced a novel snow depth inversion method using GNSS tri-frequency carrier phases. This method leverages a density-based spatial clustering approach combined with noise algorithms and reflective surface topography features to estimate snow depth. Wan et al. [28] introduced a physical model to correct the influence of surface tilt on snow depth. Zhang et al. [29] used data from 13 GNSS stations to propose a snow depth retrieval framework considering different surface materials (dry grass, wet grass, concrete). Zhou et al. [22] and Zheng et al. [30] established height baselines for different azimuth angles for slope correction. However, topographic changes are irregular,

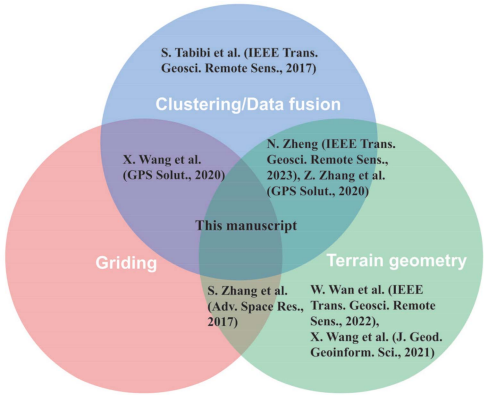


Fig. 1. Current research status of the three strategies in snow depth inversion.

| Technology | Clustering/Data fusion | Griding | Terrain geometry |
|---|---|---|---|
| Reference | ①S. Tabibi et al. (IEEE Trans. Geosci. Remote Sens.,2017) ② N. Zheng (IEEE Trans. Geosci. Remote Sens., 2023), ③ Z. Zhang et al. (GPS Solut., 2020) | ①X. Wang et al. (GPS Solut., 2020), ② S. Zhang et al. (Adv. Space Res.,2017) | ①W. Wan et al. (IEEE Trans. Geosci. Remote Sens., 2022), ②X. Wang et al. (J. Geod. Geoinform. Sci., 2021) |
| Mian purpose | ① GPS and GLONASS simulated and real signals used for snow depth monitoring. Inversion accuracy improved through weighted fusion based on uncertainty **to improve accuracy**. ②、③ Trajectory clustering **to reduce terrain impact**. Data fusion via triple frequency carrier and variance component estimation. | ①**Reduce terrain impact** on effective height inversion for each grid region. ②**Visualization method** for effective height Power Spectral Density (PSD) at different locations, selecting reliable azimuth data for robust regression estimation. | ①Continuous terrain profiles are generated around the GNSS antenna by **interpolating discrete reflector heights**, enabling slope analysis in all directions. ② The derived terrain error formula, integrating simulated reflections and SNR data, **refines slope detection and enhances terrain accuracy.** |
| VS | | | |
| Mian purpose in this manuscript | Analying spatio-temporal availability of Multi-GNSS signals around site **to improve spatio-temporal resolution** of inversion results. | Adopted grid-based modeling approach from ① **for multi-GNSS data fusion**. First Peak Ratio Weighting (PRW) fusion of single system signals within grids, then inverse distance weighted fusion of multi-GNSS signals. | Utilizing the terrain error formula from ② **as a method to account for local micro-topography**, we introduce DEM data to directly adjust SNR signals, offering greater accuracy and higher spatial resolution |

Fig. 2. Differences between this article and existing research.

and the topography within each azimuth angle doesn't remain consistent.

In summary, terrain error is a major factor affecting snow depth inversion accuracy, while multi-GNSS data availability provides the basis by ensuring coverage (spatial resolution) and revisit rate (temporal resolution) surrounding the site. However, each reflected signal has a different effective reflection footprint, and is affected by anisotropic terrain, posing huge challenges for high spatial resolution snow depth inversion and requiring consideration of microtopography influences on each effective reflection zone. Therefore, we need to correct terrain errors in order to ensure reliability of the GNSS signals in each reflection zone. After obtaining abundant reliable high spatiotemporal resolution reflected signals, how to fuse the multi-GNSS signals is key. Although some studies have examined terrain geometry, clustering/data fusion, and grid-based modeling, as Fig. 1 shows, they have not addressed terrain error impacts and multi-GNSS data fusion simultaneously—which is necessary for high spatiotemporal resolution, accurate snow depth estimation. Building on this, our study adapts existing research methodologies for distinct purposes, as illustrated in Fig. 2, to achieve high spatiotemporal resolution snow depth inversion from the following four aspects:

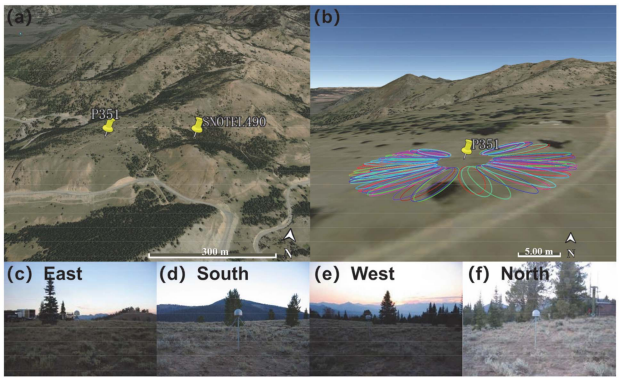


Fig. 3. Surrounding environment of site P351. (a) Locations of P351 and Station SNOTEL490. (b) Effective monitoring area of P351. (c) Eastern side of Station P351. (d) Southern side of P351. (e) Western side of P351. (f) Northern side of P351.

1) The temporal and spatial reproducibility of multi-GNSS signals and their accuracy analysis.
2) Microterrain error correction for reflected signals based on digital elevation model (DEM).
3) Data fusion methods for single-system, single-frequency satellite data based on signal peak ratio weighting (PRW).
4) Multisystem data fusion methods based on a grid approach.

The rest of this article is structured as follows: Section II introduces the experimental data and site conditions surrounding the observation area. Section III presents the proposed multi-GNSS-IR snow depth inversion method with high temporal and spatial resolution that incorporates terrain error correction. The necessity of this method for snow depth study is analyzed using both simulated and field data. In Section IV, the effectiveness of the proposed method is verified using field data, and its generalizability is further validated using data from other sites. Finally, Section V summarizes the key contributions.

## II. Site and Dataset

In this study, GNSS observation data from site P351, a part of the plate boundary observatory (PBO), situated in central Idaho, USA (43.87441°N, 114.71916°W) at an elevation of 2692.6 m, was utilized. Its altitude leads to over 200 days of snow coverage annually. The site employs the SEPT POLARX5 receiver and the Trimble Choke Ring w/Tallysman LNA antenna, with a data sampling rate of every 15 s. Snow depth references were sourced from the snow telemetry (SNOTEL) station 490,[1] positioned northwest of P351 (43.87497°N, 114.71363°W). Fig. 3 depicts the environment around P351, showcasing prominent terrain variations and limited vegetation, with only a few trees that might marginally affect signal reception at certain azimuths. This setting meets the criteria for conducting snow depth inversion at high spatiotemporal resolutions. GNSS data from P351 spanning day of the year (DOY) 193 of 2020 to DOY 180 of 2021 was analyzed. Notably, the median antenna height during the snow-free period of DOY 193 to DOY 233 in 2020 was considered as the station's antenna height. Data from DOY 240 in 2020 to DOY 180 in 2021 contributed to the snow depth inversion.

[1]Online. [Available]: https://wcc.sc.egov.usda.gov/reportGenerator/

## III. Terrain-Corrected Multi-GNSS-IR Method for High-Resolution Snow Depth Inversion

We implemented the proposed high spatiotemporal resolution snow depth inversion solution with Multi-GNSS-IR in complex terrain following the flowchart in Fig. 4.

### A. Principle of Snow Depth Inversion Using GNSS-IR and the Impact of Terrain Errors

Fig. 5 illustrates the geometric model of GNSS-IR. In Fig. 5(a), where the surface is horizontal, $e$ is the incident angle, and the path delay of the reflected signal relative to the direct signal is $\delta s = D1 - D2$. When the surface is tilted, assuming the tilt angle of the reflecting surface is $\theta$, as shown in Fig. 5(b), the incident angle $g$ is as follows:

$$g = e + \theta. \tag{1}$$

$H$ and $H_t$ represent the vertical distances from the horizontal reflecting surface and the tilted reflecting surface to the antenna phase center, respectively.

Based on the geometric model, the path delay of the reflected signal relative to the incident signal is as follows:

$$\delta s = D1 - D2 = \frac{H_t}{\sin g} - \frac{H_t \cos 2g}{\sin g} = 2H_t \sin g. \tag{2}$$

The carrier phase offset between the reflected signal and the direct signal is as follows:

$$\delta\varphi(t) = \frac{2\pi}{\lambda}\delta s = \frac{4\pi H_t \sin g}{\lambda} \tag{3}$$

where $\lambda$ denotes the wavelength of the GNSS carrier.

The reflected signal SNR is as follows:

$$\mathrm{SNR}_r = \cos\delta_\varphi(t)\frac{2A_dA_r}{N_0} = \frac{2A_dA_r}{N_0}\cos\left(\frac{4\pi H_t \sin g}{\lambda}\right) \tag{4}$$

where $A_d$ represents the amplitude of the direct signal, and $A_r$ represents the amplitude of the reflected signal. For most receivers, the value of is –205 dBW/Hz.

$\mathrm{SNR}_r$ can be simplified as a cosine function:

$$\mathrm{SNR}_r = A_x \cos(2\pi f_t x_t) \tag{5}$$

where the frequency of the function is $f_t = 2H_t/\lambda$, and the variable is $x_t = \sin g$.

The frequency $f_t$ of $\mathrm{SNR}_r$ can also be obtained by spectral analysis, thereby the antenna height $H_t$ can be calculated as follows:

$$H_t = \lambda f_t/2. \tag{6}$$

$H_{Gt}$ is the distance from the receiver antenna phase center to the bare reflecting surface. After snowfall, the distance $H_{St}$ from the receiver antenna phase center to the snow surface can

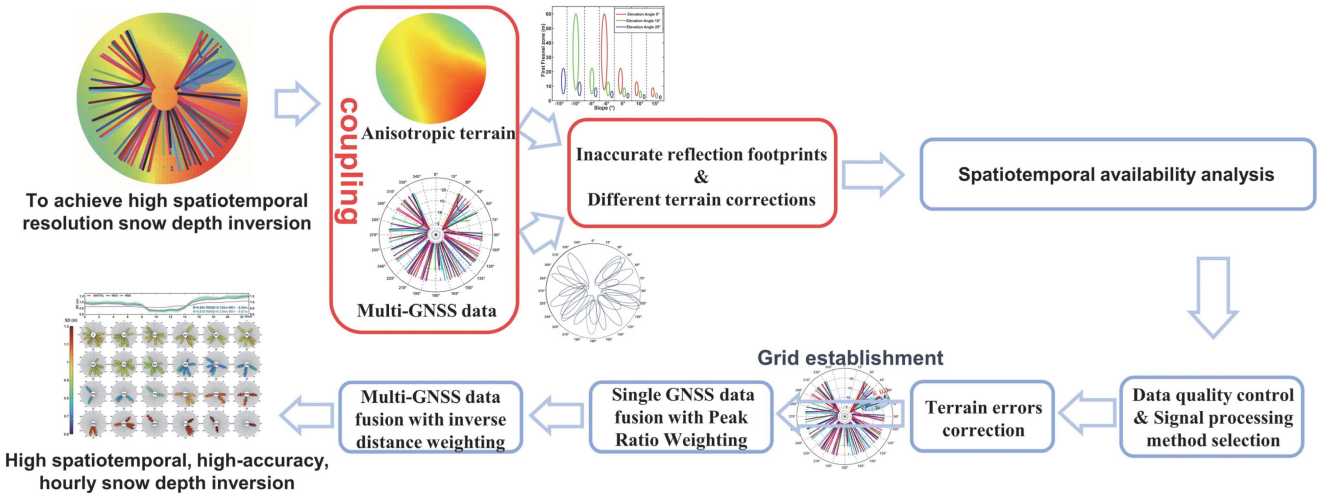


Fig. 4. Flowchart of the proposed solution for high spatiotemporal resolution snow depth inversion.

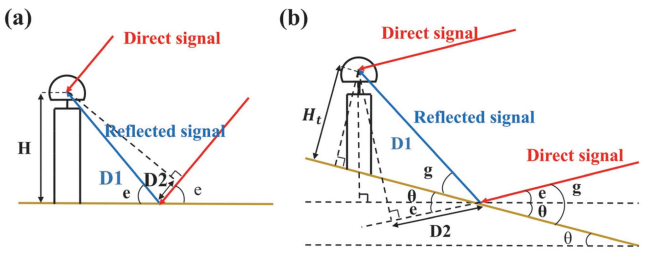


Fig. 5. Geometric model of GNSS-IR snow depth inversion. (a) Schematic of the geometric model when the surface is horizontal. (b) Schematic of the geometric model when the surface is tilted.

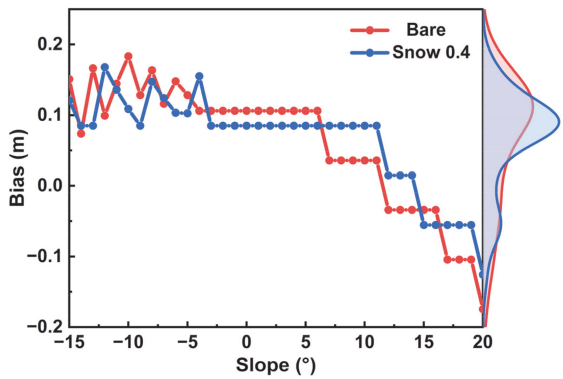


Fig. 6. Influence of terrain on snow depth inversion.

be calculated using the same method, and the snow depth $\mathrm{SD}_t$ is as follows:

$$\mathrm{SD}_t = H_{Gt} - H_{St} = \frac{\lambda\left(f_{Gt} - f_{St}\right)}{2}. \tag{7}$$

As shown in (1)–(6), snow depth $\mathrm{SD}_t$ can be calculated as long as the terrain slope $\theta$ is known. The terrain slope $\theta$ at different locations surrounding the station can be computed based on the DEM.

*1) Analysis of Terrain Errors and Correction Algorithm:* Many studies did not focus the influence of the terrain surrounding GNSS observation stations. In this research, based on a forward propagation physical model, we simulated SNR data for scenarios with an effective antenna height of 2 m, terrain slopes ranging from –15° to 20°, and two different surface conditions: bare ground and snow depth of 0.4 m. We then plotted the inversion errors in Fig. 6. Fig. 6 shows clear differences in inversion errors between snow-free periods and snowy periods. However, in practical inversion processes, the impact of terrain on antenna height during spectral analysis is often disregarded, which to some extent affects the accuracy of the inversion.

As an example, we selected GNSS data from the P351 and GPS satellite PRN1 S2L for DOY 190 of the year 2020. We analyzed the influence of terrain on the reflected signal for satellites with a slope of 5° and azimuths between 30° and 60°, as shown in Fig. 7. In Fig. 7(a), the red line represents the SNR reflected signal before terrain error correction, while the blue line represents the SNR reflected signal after terrain error correction. It is evident that, compared to the signal before correction, the signal after terrain error correction shifts noticeably to the right along the $x$-axis. The horizontal coordinate range corresponding to the signal before terrain error correction is approximately $\sin(25°) - \sin(5°) \approx 0.335$, whereas the horizontal coordinate range corresponding to the signal after terrain error correction is approximately $\sin(30°) - \sin(10°) \approx 0.326$. It can be observed that the frequency $\omega_t$ of the signal after terrain error correction becomes higher than that of the signal before correction, as $\sin(30°) - \sin(10°) < \sin(25°) - \sin(5°)$. The spectral analysis plots before and after correction are shown in Fig. 7(b), where the red line represents the spectrum analysis before correction, and the blue line represents the spectrum analysis after correction. Similarly, the spectral curve after correction is shifted to the right relative to the one before correction, and the difference in antenna height corresponding to the peak value of the spectrum after correction and the antenna height before correction is

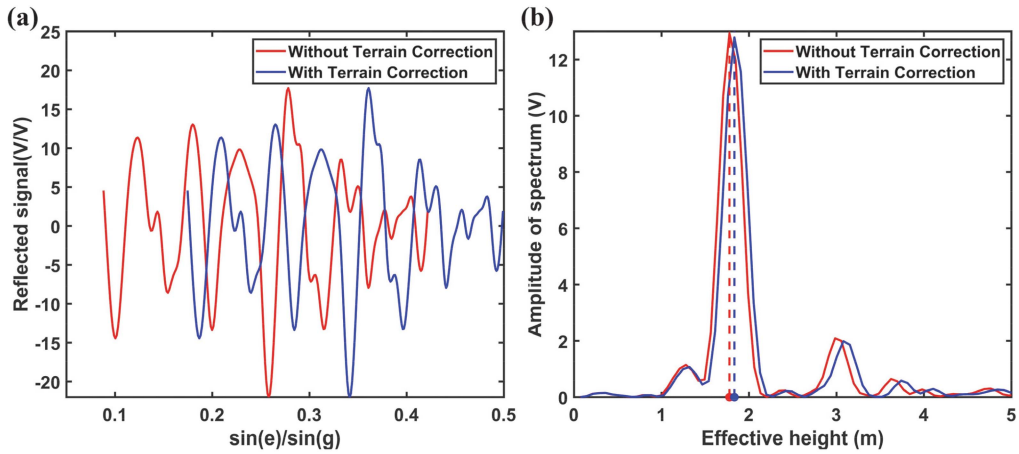


Fig. 7. Influence of terrain error correction on the reflected signal. (a) Comparison of SNR reflected signals before and after terrain error correction. (b) Comparison of spectral analysis before and after terrain error correction.

approximately 6 cm. Errors caused by significant terrain slopes at stations with steep slopes cannot be ignored, highlighting the necessity of terrain error correction during GNSS-IR snow depth inversion.

### *B. Analysis of GNSS Track Availability and Reflective Region Variations*

To enhance the spatiotemporal resolution of GNSS-IR snow depth inversion, it is imperative to comprehensively utilize multisystem GNSS signals. Classical snow depth inversion methods did not consider terrain anisotropy or the spatiotemporal reproducibility characteristics and data quality from different satellites impacting the inversion results. To improve GNSS data utilization rate and achieve high spatiotemporal resolution inversion while avoiding system errors between different satellites and trajectories, this study preprocesses SNR sequence data. This includes obtaining starting azimuth angle, ending azimuth angle, starting elevation angle, ending elevation angle, and the median values of azimuth and elevation angles for each SNR sequence. These are then classified by satellite sequence numbers. Subsequently, based on starting and ending elevation angles, the SNR sequences are divided into ascending and descending trajectories. Lastly, SNR sequence data with similar trajectories (those starting within 5° of each other—this value can be determined according to the desired spatiotemporal resolution) are grouped. The multi-GNSS signals used in this paper all come from MEO satellites. The satellite orbital altitudes are as follows: for the GPS system, 20,200 km with an operational period of 11 h 58 min and a revisit period of 1 day; for the GLONASS system, 23 616 km with an operational period of 14 h 4 min and a revisit period of 11 days; for the Galileo system, 23 616 km with an operational period of 14 h 4 min and a revisit period of 11 days; and for the BeiDou system, 21 528 km with an operational period of 12 h 50 min and a revisit period of 7 days. It is worth mentioning that if the ground station can receive data from BeiDou navigation satellite system (BDS) IGSO and GEO satellites, their data availability needs further consideration [31], [32].

*1) Analysis of GPS Satellite Track Availability:* The site P351 used in this section can receive the L1C and L1W signals of the GPS satellite's L1 band, the L2L and L2W signals of the L2 band, and the L5Q signal of the L5 band. Previous studies [14], [15], [33] have shown that the L1W and L2W are not effective for snow depth inversion; hence, only the L1C, L2L, and L5Q signals are used. To distinguish different satellite systems, GPS satellites are represented with "G" instead of PRN, e.g., G1 represents PRN 1 of the GPS system. GLONASS satellites are denoted by R, Galileo by E, and BDS by C. Due to data gaps, preprocessing is required before inversion. The required SNR observations of S1C, S2L, and S5Q from the L1C, L2L, and L5Q bands respectively are extracted from the observation file. Satellite navigation files and observation files are used to compute the elevation and azimuth angle information of the satellite concerning the station. It was found that out of 32 GPS satellites during the selected period, most satellites did not have data gaps. However, satellites G11, 14, and 23 were missing data for over 50 days, affecting subsequent inversions. After extracting SNR observations from all satellites, it was found that all 32 satellites had S1C values, 21 satellites had S2L (excluding G2, 11, 13, 14, 16, 18, 19, 20, 21, 22, 23), and only 13 satellites (G1, 3, 4, 6, 8, 9, 10, 24, 25, 26, 27, 30, 32) had S5Q values. The selected satellite elevation angle range for this study was 5°–25°.

We excluded satellites with trajectory differences between snow-free and snow periods during classification. Ultimately, 21 satellites with a total of 58 trajectories were selected, including 29 ascending and 29 descending trajectories. Trajectory diagrams of a single satellite and all satellites for the GPS system are shown in Fig. 8. Fig. 8(a) displays the trajectory of satellite G8. It can be observed that the G8 satellite has four trajectories. Two ascending trajectories are around azimuth angles of 137.7° and 320.5°, represented by upright triangles, while two descending trajectories are approximately at 42.4° and 245.4°, depicted by inverted triangles. Fig. 8(b) shows trajectories of all GPS satellites; the $x$-axis represents satellite sequence numbers with positive values for ascending trajectories and negative for descending trajectories. The $y$-axis represents

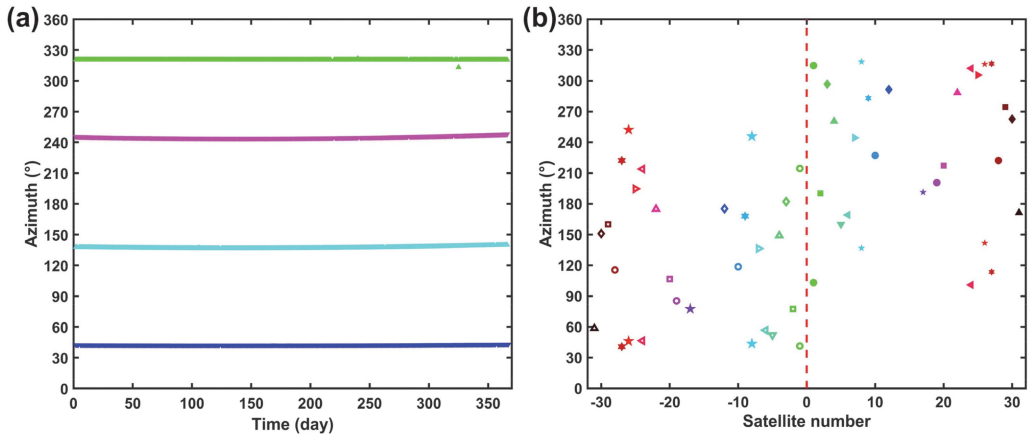


Fig. 8. Trajectory diagrams of a single satellite and all satellites for the GPS system. (a) Trajectory diagrams of satellite G8. (b) Trajectory diagrams of all GPS satellites.

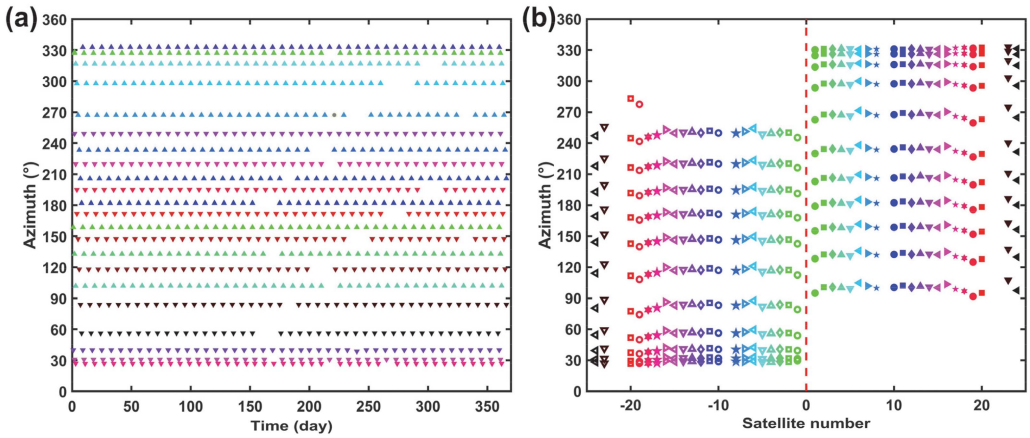


Fig. 9. Trajectory diagrams of a single satellite and all satellites for the GLONASS system. (a) Trajectory diagrams of satellite R1. (b) Trajectory diagrams of all GLONASS satellites.

the median azimuth angles of all satellite trajectories. Different colors and shapes symbolize different GPS satellites, with solid shapes indicating ascending trajectories and hollow shapes indicating descending. Noticeably, there are no trajectories between azimuth angles 0°–30° and 330°–360°. Descending trajectories are primarily between 30° and 90°, and most between 270° and 330° are ascending, with just one descending. Trajectories are fairly evenly distributed in other azimuth ranges. Considering the total trajectory distribution across all azimuth angles, each range has at least four trajectories, with some having up to eight trajectories.

*2) Analysis of GLONASS Satellite Track Availability:* The site P351 can receive signals from 24 GLONASS satellites. All of these satellites can emit R1 band signals, and the receiver received the S1C and S1P signals from all 24 satellites. Apart from satellites R6 and R10, the other 22 satellites can also emit S2C and S2P signals in the G2 band. In subsequent experiments, snow depth inversion was performed using the four SNR data types: S1C, S1P, S2C, and S2P. Preprocessing revealed trajectory variation issues with satellites R9, R21, and R22, so data from these three satellites was not used. Due to different inclination angles and orbital periods, GLONASS satellite trajectories differ significantly from GPS trajectories. Fig. 9 shows the trajectories for a single GLONASS satellite and all GLONASS satellites.

Fig. 9(a) shows that satellite R1 has 22 trajectories, with 11 ascending and 11 descending orbits. These trajectories are fairly distributed. Due to the large inclination angles of GLONASS orbits, trajectories are present near 30° and 330° azimuth, unlike GPS. As seen in Fig. 9(b), the azimuth angle differences between two adjacent ascending or descending trajectories for the same satellite are approximately consistent, around 30°. Different satellites have consistent trajectory distributions, with overall azimuth angle differences within 10°. It's noticeable that the trajectory counts within 0°–30°, 30°–90°, 270°–300°, and 330°–360° azimuth ranges are fewer, with counts of 24, 21, 24, and 22, respectively. The 30°–60° and 180°–210° ranges have more trajectories, with counts of 60 and 58, respectively. Other ranges have 40–50 trajectories.

*3) Analysis of Galileo Satellite Track Availability:* The receiver at the site P351 can receive signals from 21 satellites within the Galileo system, specifically satellites E1-5, E7-9, E11-13, E15, E19, E21, E24-27, E30, E31, and E33. The receiver

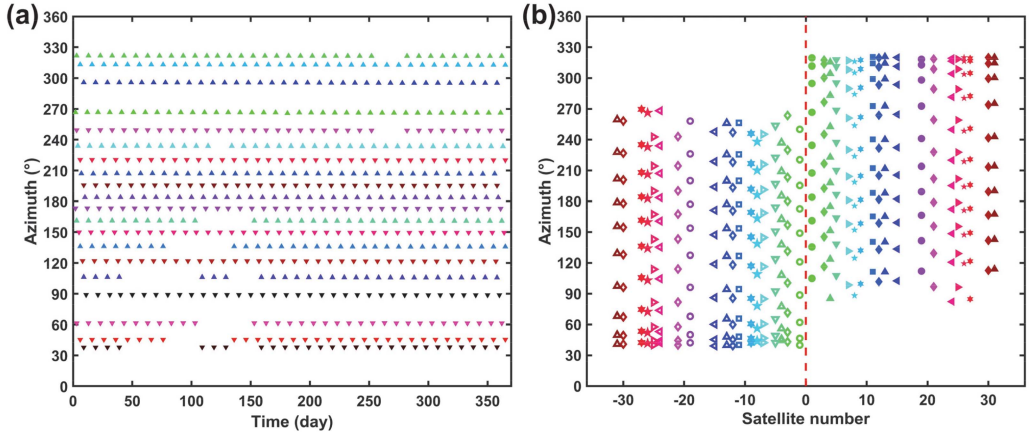


Fig. 10. Trajectory diagrams of a single satellite and all satellites for the Galileo system. (a) Trajectory diagrams of satellite E1. (b) Trajectory diagrams of all Galileo satellites.

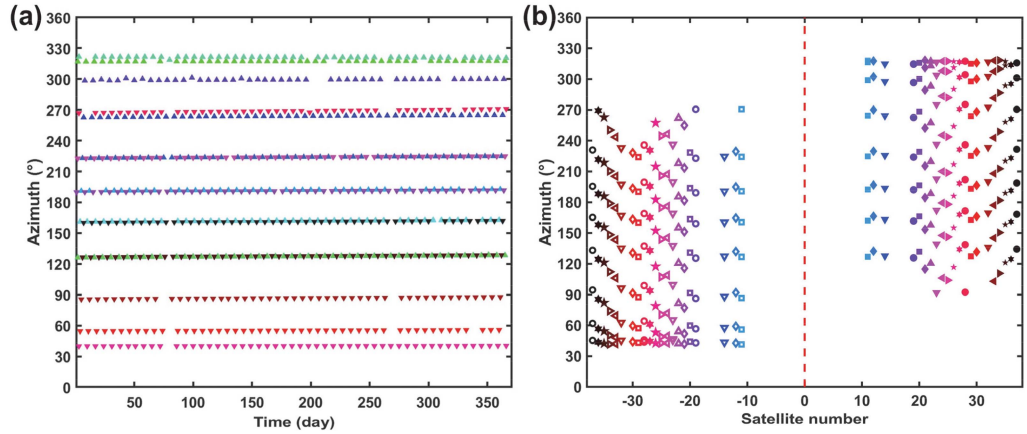


Fig. 11. Trajectory diagrams of a single satellite and all satellites for the BDS system. (a) Trajectory diagrams of satellite C11. (b) Trajectory diagrams of all BDS satellites.

can pick up the S1C signals in the E1 band, S5Q signals in the E5a band, S7Q signals in the E5b band, S8Q signals in the E5 (E5a+E5b) band, and S6C signals in the E6 band from these satellites. Therefore, five types of SNR data were used for snow depth inversion. Compared to the GPS and GLONASS systems, the trajectories of the Galileo system are more scattered, with less clear inter-satellite trajectory relationships. Due to substantial data gaps in satellites E2 and E33, only 19 satellites were ultimately used for inversion. The trajectory plots of the E1 satellite and all 21 Galileo satellites are shown in Fig. 10.

In Fig. 10, the 19 Galileo satellites used for inversion have a total of 364 trajectories. The trajectory counts in the 60°–90° and 270°–300° ranges are fewer, with 26 and 22, respectively. Other azimuth ranges contain between 30 and 50 trajectories.

*4) Analysis of BDS Satellite Track Availability:* The site P351 receiver can receive signals from 21 BDS satellites. Specifically, satellites C11, C12, and C14 have data in the B1–2 band's S2I, the B3 band's S6I, and the B2b band's S7I. Satellites B19–B30 and B32–B37 possess data in the B1 band's S1P, the B1–2 band's S2I, the B2a band's S5P, and the B3 band's S6I. The trajectory plots for the C11 satellite and all 21 BDS system satellites are shown in Fig. 11.

Fig. 11 shows the 18 BDS satellites had a total of 320 trajectories. The trajectory counts within the 60°–90°, 90°–120°,210°–240°, and 240°–270° ranges are fewer, with 18, 22, 25, and 20, respectively. Other azimuth ranges have an average of about 40 trajectories.

*5) Analysis of Effective Reflection Zone Variations:* As satellite trajectories vary, Fresnel reflection zones also change continuously. These regions are influenced not only by satellite elevation angles but also by surface slope and variations in snow depth, as demonstrated in Fig. 12. Fig. 12(a) displays the variations in the Fresnel reflection zones at a 2 m antenna height under different elevation and slope angles. The red, green, and blue ellipses in the figure represent the Fresnel reflection zones at elevation angles of 5°, 15°, and 25°, respectively. Different slope angles of the Fresnel reflection zones are separated by black dashed lines, with the $x$-axis representing the slope angle, which varies from –15° to 15° in 5° increments. At –15° slope, there is only a blue ellipse, and at –10° and –5° only blue and green ellipses are present. This occurs because the receiver

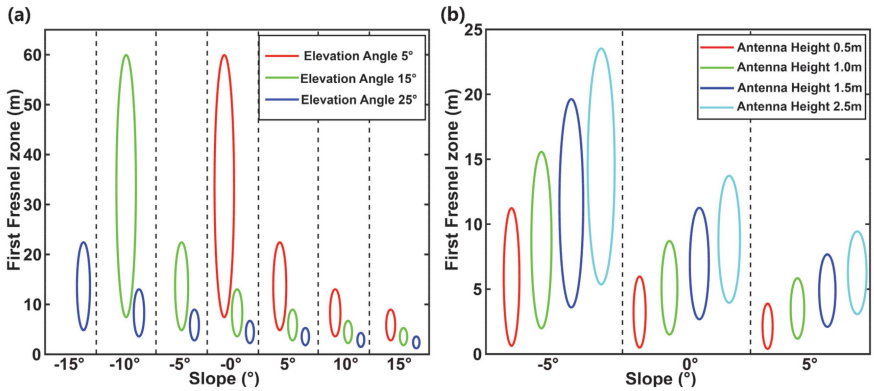


Fig. 12. Variations of Fresnel reflection zone. (a) Variation of the Fresnel reflection zone with elevation angle. (b) Variation of the Fresnel reflection zone with inclination angle.

cannot receive satellite signals at those slopes. Fig. 12(a) also demonstrates that the size of the Fresnel reflection zone is significantly affected by surface slope. Furthermore, Fresnel reflection zone size is directly proportional to antenna height. As snow accumulates, antenna height decreases along with Fresnel reflection zone size. Fig. 12(b) shows that the variations in the Fresnel reflection zone at a 15° elevation angle, considering antenna height and surface slope. From Fig. 12, a refined snow depth inversion algorithm that takes into account surface characteristics and changes in the effective reflection area is of paramount importance.

### C. High Spatiotemporal Resolution Snow Depth Fusion Inversion Method

*1) Data Quality Control:* To address the issue of reflected signal disturbances caused by environmental noise and base thermal noise, we employed various advanced signal decomposition methods to more accurately extract the reflected signal components, laying the foundation for subsequent spectral analysis and snow depth inversion. Specifically, we adopted a second-order polynomial fitting [34], [35] to capture the main trends in the SNR data; in the wavelet transform (WT) [22], [36], [37], we used the coif5 wavelet base from the Coiflet wavelet family to handle signal edges and denoise; in VMD [38], [39], [40], the Lagrange multiplier was set to 0.01, the penalty factor was set to 1000, and the number of modes was set to 9; in the complete ensemble empirical mode decomposition (CEEMD) method [41], we introduced a white noise amplitude of 0.2 and averaged it 20 times to balance reconstruction accuracy and computational complexity. These optimized parameters ensure efficiency and accuracy under various data conditions.

We implemented data quality control with precision control criteria illustrated in Table I. In Table I, the mean elevation angle, representing the average between the starting and ending elevation angles for that segment. Since the "double-peak" phenomenon [42], [43] frequently occurs during spectral analysis of the reflected signal, which severely affects the extraction of the main frequency, the peak ratio, representing the ratio between the primary and secondary peak values, serves as a quality control

TABLE I
QUALITY CONTROL PARAMETERS OF REFLECTED SIGNALS

| Quality Control Parameters | Parameter Range |
|---|---|
| Mean elevation angle | >= 10° |
| Peak ratio | >= 2.8 |
| Signal quantity | >= 50 |

criterion that can better filter out the double-peak phenomenon to some extent; the higher the secondary peak, the smaller the peak ratio. Signal quantity is the SNR signal counts of a reflection signal segment.

*2) Single-System Single-Frequency Data Fusion Method With Signal Peak Ratio Weighting:* Though data were preliminarily filtered based on the peak ratio during quality control, this step merely aims to eliminate potential gross errors. The data after filtration may still contain certain inaccuracies. A higher peak ratio corresponding to the inversed antenna height means better data quality. If the peak ratio of inversed snow depth is close to the set value during preliminary screening, the accuracy of the snow depth value would be relatively worse. Hence, we introduced a peak ratio linear normalization method for weighting. After the preliminary screening, the weight of the snow depth corresponding to the maximum peak ratio is set to 1, and the weight for the minimum peak ratio is set to 0. The weight formula $w_{p_n}$ is given as follows:

$$w_{p_n} = \frac{p_n - p_{\min}}{p_{\max} - p_{\min}} \tag{8}$$

where $p_n$ is the peak ratio corresponding to the antenna height inversed by the $n$th set of data, $p_{\max}$ is the maximum peak ratio, and $p_{\min}$ is the screening threshold. Snow depth inversion value after terrain correction is normalized and fused by peak ratio weighting to obtain single-system results.

*3) Multi-GNSS Weighted Fusion Snow Depth Inversion Based on Grid Method:* To further improve spatiotemporal resolution after acquiring high-precision single-system results, we proposed a weighted fusion of the terrain-corrected, single-frequency snow depth inversion results for the four GNSS systems through grid-based methods. After the terrain error

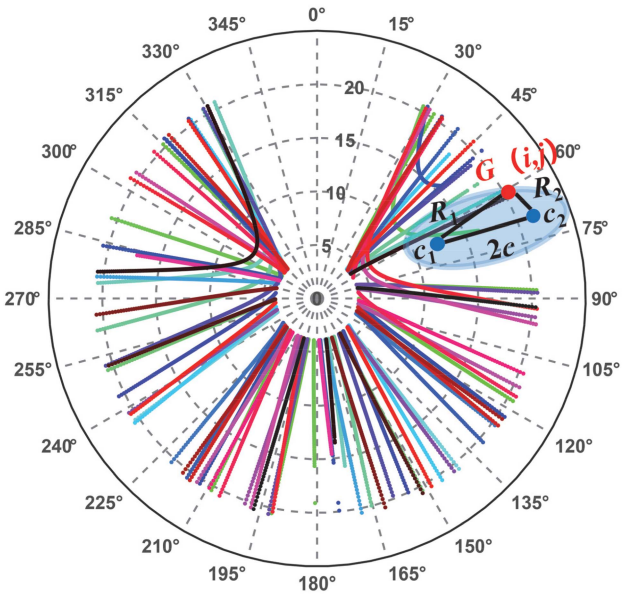


Fig. 13. Principle of the gridding method.

correction, for each reflected arc segment, we obtain its median elevation angle, median azimuth angle, and the inclination angle corresponding to the median azimuth angle. The snow depth value inversed from the $n$th reflected arc segment is denoted as $G_n$.The position of the Fresnel reflection zone can be calculated based on the information corresponding to that arc segment.

The steps for snow depth inversion through grid-based multisystem fusion are as follows: First, the area surrounding the site is processed using a polar coordinate grid system, with the site's location serving as the center of the polar coordinates. Based on the precision requirements, the effective reflection zones are delineated. Subsequently, the positions of all arc segments within the Fresnel reflection zones are determined. Fig. 13 shows an example of a 5 m × 15° grid. Traverse all grids and match them with the reflection zones. Every grid is matched with the reflection zones, and the snow depth inversion values corresponding to each reflection zone within the grid are weighted to obtain the SD$(i, j)$:

$$\mathrm{SD}\,(i,j) = \frac{\sum_{n=1}^{N} w_n \cdot G_n}{\sum_{n=1}^{N} w_n} \tag{9}$$

where $w_n$ is the weight of $G_n$, and the calculation formula for $w_n$ is as follows:

$$w_n = 1 - \frac{D - 2c_n}{2a_n - 2c_n} \tag{10}$$

where $D$ represents the sum of the distances from the grid point to the two foci of the Fresnel reflection zone, $2c_n$ is the focal length of the ellipse, and $a_n$ is the semi-major axis of the ellipse.

The snow depth inversion value B for a single day is the average of the snow depths of all grid points, calculated as follows:

$$\mathrm{SD}_g = \mathrm{mean}\,(\mathrm{SD}\,(i,j))\,. \tag{11}$$

TABLE II
RESULTS OF FOUR REFLECTION SIGNAL EXTRACTION METHODS

| Method | Arc segments count | Utilization | Improvement rate | R | RMSE (m) |
|---|---|---|---|---|---|
| LOPF | 10717 | 46.88% | - | 0.972 | 0.226 |
| WT | 12488 | 54.63% | 16.53% | 0.978 | 0.203 |
| CFEMD | 12686 | 55.50% | 18.37% | 0.982 | 0.198 |
| YMD | 13930 | 60.94% | 29.98% | 0.977 | 0.214 |

## IV. RESULTS AND DISCUSSION

### A. Data Quality Control and Selection of Reflection Signal Extraction Method

In this experiment, we selected the SNR data from the L1 band of the GPS system from DOY 193 in 2020 to DOY 180 in 2021 at site P351 for snow depth inversion. The inversion results are shown in Table II. It can be seen from Table II that during the experimental period, 22 859 arcs were obtained from 32 satellites of the GPS system. Using the LOPF method, after quality control, the number of arc segments remaining was 10 717, with a data utilization rate of 46.88%. When employing WT, CEEMD, and VMD methods, the number of usable arc segments after quality control were 12 488, 12 686, and 13 930, respectively, with data utilization rates of 54.63%, 55.50%, and 60.94%, respectively. It is obvious that compared to the LOPF method, the three SNR reflection signal extraction methods can improve the data utilization rate by 16.53%, 18.37%, and 29.98%, respectively. The inversion results of all four methods can effectively capture the trend in snow depth changes. However, the traditional LOPF method yielded relatively inferior results, with a correlation coefficient ($R$) value of 0.831 and root mean square error (RMSE) of 0.088 m. In contrast, the WT, CEEMD, and VMD methods have shown significant improvements over the LOPF. Among them, the CEEMD method performed the best, with an $R$ value of 0.932 and RMSE of 0.07 m, reducing the RMSE of the LOPF by 0.018 m, an improvement of 20.5%. This proves that these three methods can address the multipeak problem in spectral analysis to a certain extent. Among these three methods, the VMD method had the best improvement in data utilization rate but with minimal accuracy improvement. Overall, CEEMD seems to be the better choice. Hence, in the following experiments, the CEEMD method was chosen for extracting reflection signals.

### B. Visibility of GNSS Trajectories and Their Inversion Results

Although, theoretically, one trajectory is enough to inversely derive snow depth, not all trajectories can effectively yield snow depth due to signal quality issues. After conducting experiments on the data from various trajectories, it was found that the azimuth angle location has a significant impact on snow depth inversion. Additionally, the revisit cycles of satellites from different GNSS systems vary. Therefore, based on the visibility of GNSS satellite trajectories, we segmented the data at intervals of 5° for clustering. Using classical methods, we inversed all GNSS data of P351 station from the DOY 193 in 2020 to the DOY 180 in 2021. The inversion results for each system every five degrees and their trajectory counts are shown in Fig. 14.

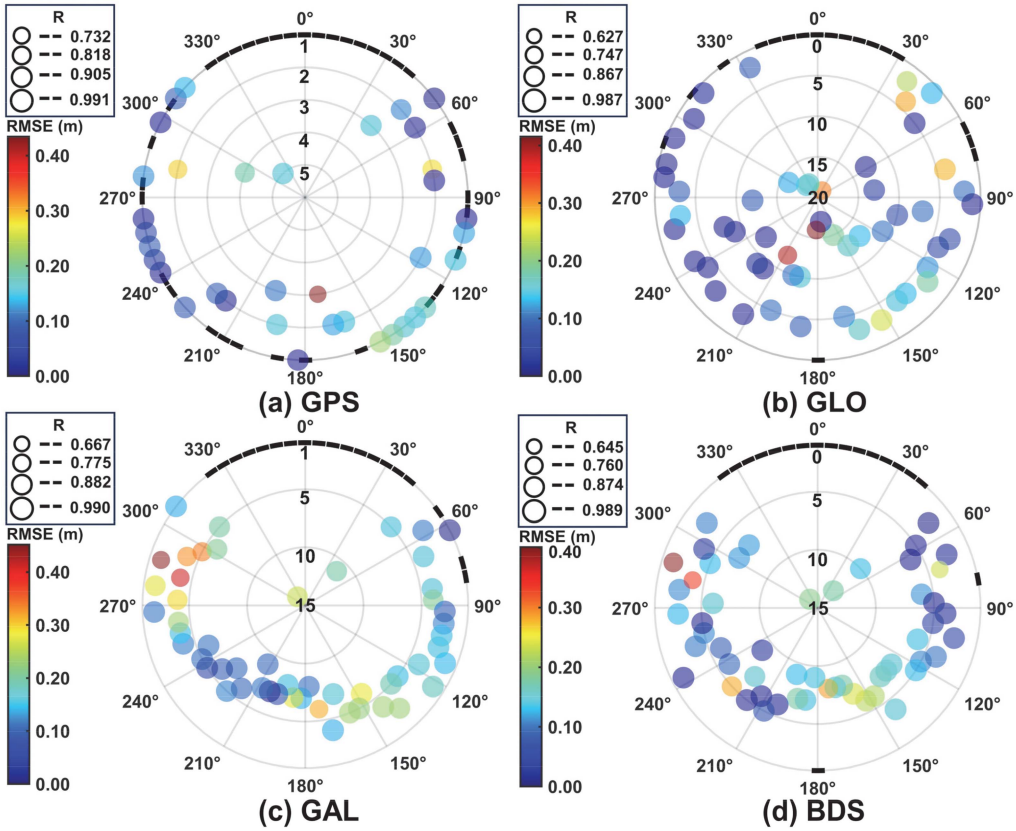


Fig. 14. GNSS snow depth inversion results based on the classical method. (a) Inversion results of the GPS system. (b) Inversion results of the GLONASS system. (c) Inversion results of the Galileo system. (d) Inversion results of the BDS system.

The size of the circles in the figure indicates the $R$ value of this interval, the color represents the RMSE, and the radial length indicates the number of GNSS trajectories. Azimuth angles with no satellite reflection signals are represented by a bold black line on the outermost part of the figure.

From Fig. 14(a), the GPS system has 60 available trajectories, of which 19 trajectories located in the azimuth angle intervals of 55°–75°, 85°–100°, 215°–260°, and 300°–310° exhibit good inversion results. Their mean $R$ value is above 0.97, with an RMSE consistently less than 0.16 m, making up 31.67% of the available trajectories. Fig. 14(b) shows that the GLONASS system data generally provides better inversion results, with a substantial number of available trajectories reaching 380. Among them, 160 trajectories within the azimuth angle ranges of 55°–75°, 105°–120°, 205°–260°, 270°–295°, and 305°–315° yield inversion results with an RMSE below 0.16 m, constituting 42.11% of the available trajectories. In Fig. 14(c), the Galileo system's inversion accuracy is somewhat lacking, especially in the 260°–320° interval. However, it compensates for the shortcomings of the GPS and GLONASS systems, which display lower inversion accuracy and fewer available trajectories in the 150°–210° range. From Fig. 11(d), the BDS system's performance exhibits smaller fluctuations, similar to GLONASS, but higher accuracy between 50° and 100°.

### C. Analysis of Single Frequency GNSS Signal Inversion Results

Due to factors such as signal strength, the inversion accuracy of signals from various bands is not uniform. The combination of multi-GNSS may not necessarily improve snow depth inversion accuracy. Consequently, we compared the inversion accuracy of individual band signals, as shown in Fig. 15.

For the GPS system, S1C, S2L, and S5Q SNR data can effectively be used to inverse snow depth, with $R$ values all greater than 0.98. Among them, the S2L exhibits the best snow depth inversion performance with an $R$ of 0.987, RMSE of 0.175 m, and ME of –0.107 m. The S5Q is next in line in terms of effectiveness, while the S1C inversion results are relatively the least accurate. For the GLONASS system, S1C has the poorest inversion results with $R$ of 0.977 and RMSE of 0.185 m. In contrast, the S2P presents the best inversion results, registering $R$ of 0.986 and RMSE of 0.163 m. For the Galileo system, the S1C produces the best inversion results with $R$ of 0.984, RMSE of 0.17 m, and ME of –0.102 m. The S5Q displays the least impressive performance with $R$ of 0.967, RMSE of 0.224 m, and ME of –0.130 m. For the BDS system, the S2I band shows the best performance with $R$ of 0.983 and RMSE of 0.171 m, while the S5P band lags with $R$ of 0.971 and RMSE of 0.212 m.

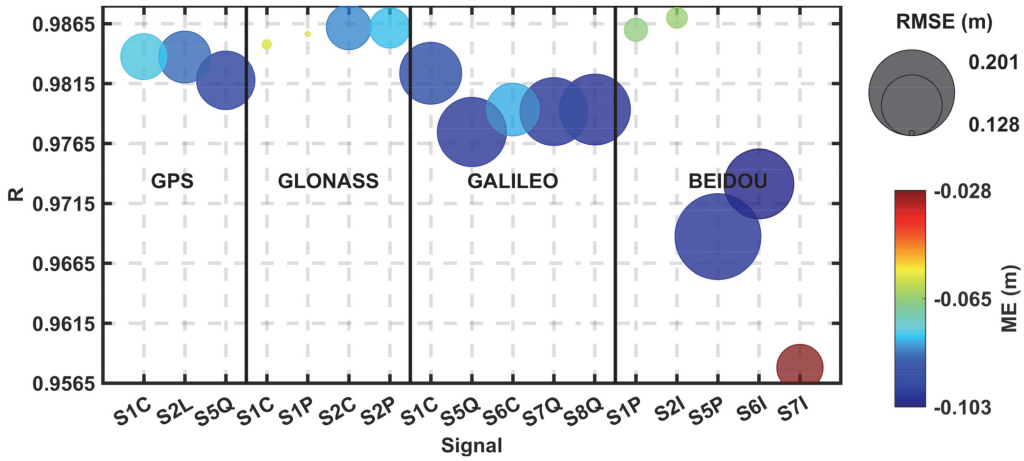


Fig. 15. Inversion accuracy of individual band signals.

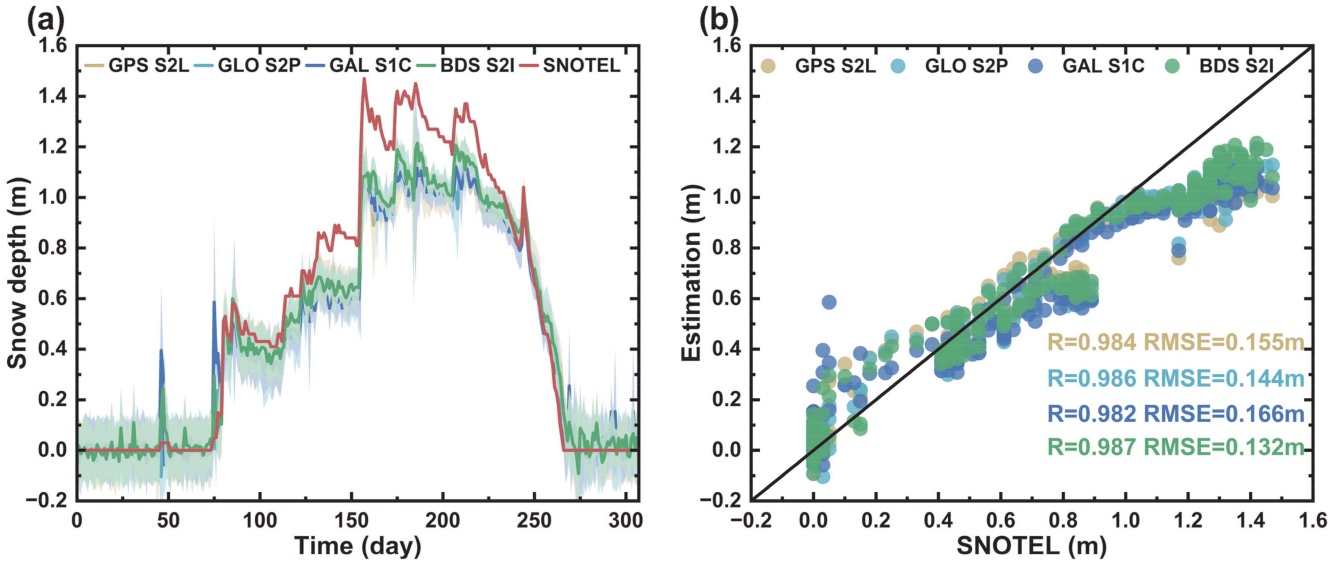


Fig. 16. Snow depth inversion results for the optimal frequency bands. (a) Inverted snow depth values and errors for the optimal frequency bands. (b) Scatter plots of the inverted values against reference values.

Furthermore, Fig. 16 shows the snow depth inversion values and their respective errors (indicated by the shade corresponding to the inversion value colors) for each system. It can be seen that the inversion results of all four systems are consistent with the reference snow depth value, effectively capturing the trends in snow depth variations. The inversion performs better when snow cover is shallow. When snow depth reaches a certain level, the inversion error increases. Notably, the Galileo system SIC signal exhibits substantial fluctuations, followed by the GPS system S2L signal. Although the GLONASS system S2P signal shows less variability, it tends to underestimate snow depth. In contrast, the BDS system S2I signal demonstrates superior performance both during snowy and nonsnowy periods. Thus, we selected GPS S2L, GLONASS S2P, Galileo S1C, and BDS S2I signals for subsequent experiments.

### D. Results of Terrain Error Correction

We computed the slope using the high-precision topographical map around the P351 site and plotted it in Fig. 17. Based on the positions of the reflection point trajectories and their corresponding slopes, we conducted a terrain error correction for the reflected signals. This correction was applied to the optimal bands of the four systems. As shown in Fig. 17, the three-dimensional (3-D) surface at the top represents the slope values around the P351 site, while the flat plane at the bottom represents the DEM values. DEM data from the USGS 1/9 arc-second digital elevation models product,[2] as part of the 3-D elevation program, has a RMSE of 0.53 m. The snow depth inversion

[2]Online. [Available]: https://cires1.colorado.edu/portal/

TABLE III
SNOW DEPTH INVERSION RESULTS WITH TERRAIN ERROR CORRECTION OF THE OPTIMAL BANDS

| Signal | Method | ME (m) | R | RMSE (m) | Improvement rate of RMSE |
|---|---|---|---|---|---|
| GPS S2L | CM | –0.086 | 0.984 | 0.155 | – |
| | TEC | –0.076 | 0.986 | 0.141 | 9.0% |
| GLO S2P | CM | –0.079 | 0.986 | 0.144 | – |
| | TEC | –0.040 | 0.982 | 0.132 | 8.3% |
| GAL S1C | CM | –0.089 | 0.982 | 0.166 | – |
| | TEC | –0.085 | 0.987 | 0.148 | 10.8% |
| BDS S2I | CM | –0.064 | 0.987 | 0.132 | – |
| | TEC | –0.038 | 0.982 | 0.122 | 7.6% |

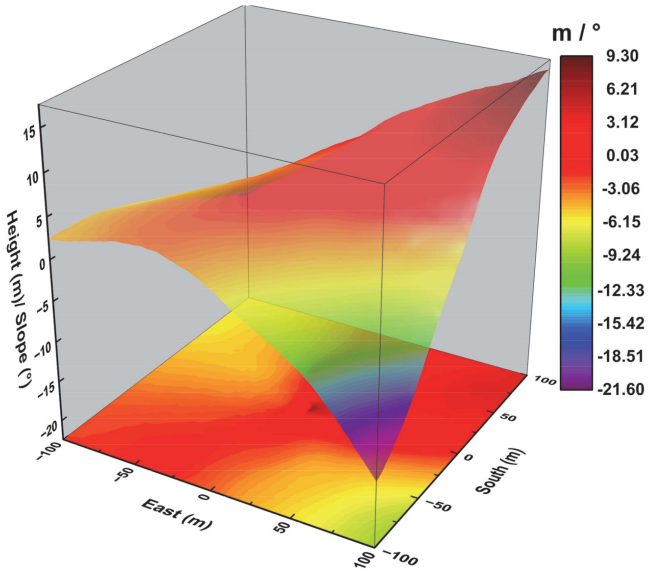


Fig. 17. DEM (bottom) and slope map (top) around the P351 site.

results for the four bands are shown in Fig. 18. Fig. 18(a) shows the snow depth inversion results after terrain correction for the SNR data from four bands. Fig. 18(b)–(e) illustrate the correlation of inversion results before and after terrain error correction. Gray circles and lines represent inversion results obtained using classical methods (CMs). To make it more noticeable, a red line is used to represent the fitting line of the inversion results after terrain error correction. It can be seen that the terrain error correction algorithm can effectively inverse snow depth, improving the accuracy of all bands. Especially in deep snow scenarios, the corrections appear more effective. From Table III, after terrain error correction (TEC), the $R$ values from snow depth inversion of the four GNSS signals are comparable to traditional methods. However, the RMSE decreased by 0.014, 0.012, 0.018, and 0.010 m, respectively, with improvement rates of 9.0%, 8.3%, 10.8%, and 7.6%. The ME decreased by 11.63%, 49.4%, 4.50%, and 40.6%. After terrain error correction, the inversion results for the BDS S2I signal are the best, followed by the GLO S1C signal. The results for the GPS signal and the GLO signal are slightly inferior.

### *E. Signal Peak Ratio Weighting (PRW)*

Within a single area, there are often multiple reflection signal trajectories from different satellites, each with varying signal qualities. To fully utilize the surface information conveyed by these multiple signals to inverse the most accurate snow depth values, we use a PRW algorithm based on terrain error correction. Peak ratio indicates data quality, with higher ratios meaning better antenna height inversion. Snow depths near the screening threshold have lower accuracy. We introduced peak ratio normalization for weighting to account for quality variations. The terrain-corrected inversions are weighted by peak ratio then fused, improving snow depth accuracy. In this section, PRW data fusion experiments were carried out based on the SNR data of the four systems for P351 from the DOY 240 in 2020 to the DOY 180 in 2021. The results are displayed in Fig. 19 and Table IV.

Fig. 19(a) presents the snow depth inversion results after PRW for the four bands. Fig. 19(b)–(e) compare the inversion results of the PRW method with those from the CM. The results indicate that the peak ratio weighting algorithm further enhances the accuracy of snow depth inversion. Compared to the terrain error correction algorithm, the RMSE decreased by 4.3%, 6.8%, 6.1%, and 7.4%, respectively. When compared to the CM there is a significant improvement in RMSE, with reductions of 12.9%, 14.6%, 16.3%, and 14.4%, respectively. Moreover, the snow depth inversion algorithm, based on terrain error correction and PRW, has comparable R values to traditional methods, but the ME decreased by 27.9%, 55.7%, 22.5%, and 64.1%. Overall, the BDS S2I signal still performed best, followed by the GLO S1C signal, with the GPS and GLO systems being slightly less effective.

To verify the applicability of the method in this article, we conducted experiments using the SNR data of GPS system L1C band from the DOY 240 of 2015 to the DOY 180 of 2016 at sites P350 and P682. Both P350 and P682 sites are part of the PBO network. The terrain around the P350 site is significantly undulating, with an approximate 10° upward slope to the west and a 6° downward slope to the southeast; the P682 site is characterized by a notable east-west inclination of about 8°, with a 5° upward slope to the south and a relatively flat northern direction. Fig. 20 and Table V compare the snow depth inversion results between the CM and the PRW method for sites P350 and P682. It can be seen that the inversion accuracy of the two sites

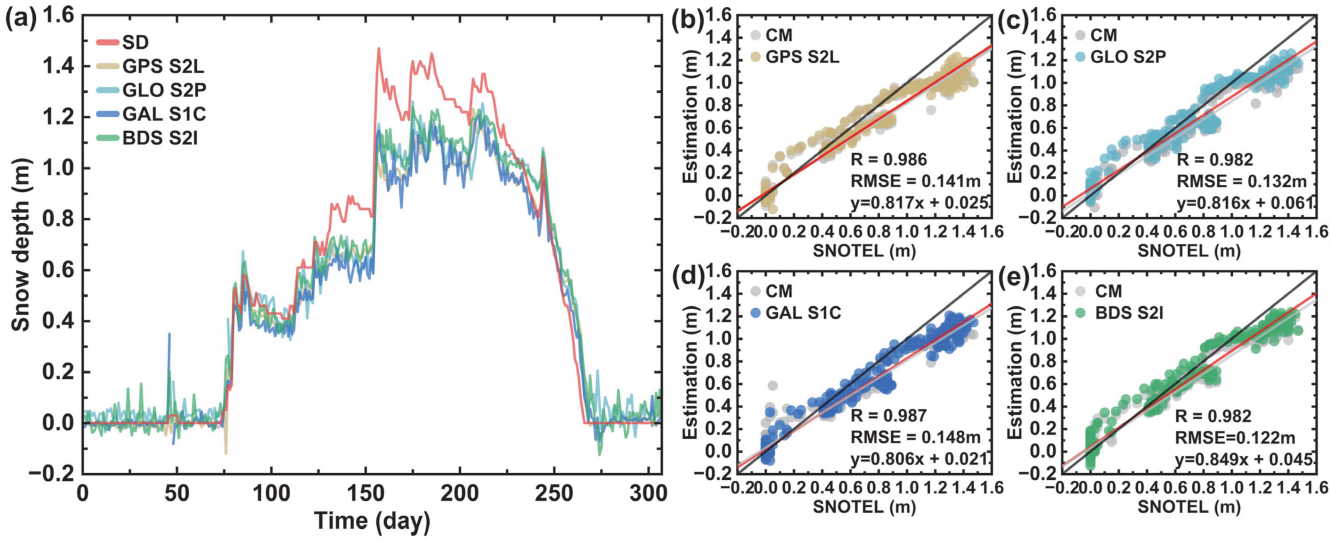


Fig. 18. Snow depth inversion results with terrain error correction of the optimal bands. (a) Time series of snow depth inversion values for the optimal bands. (b)–(e) Scatter plots of the inversion values against the SNOTEL references. SD represents the SNOTEL references. CM denotes the results of the classical method.

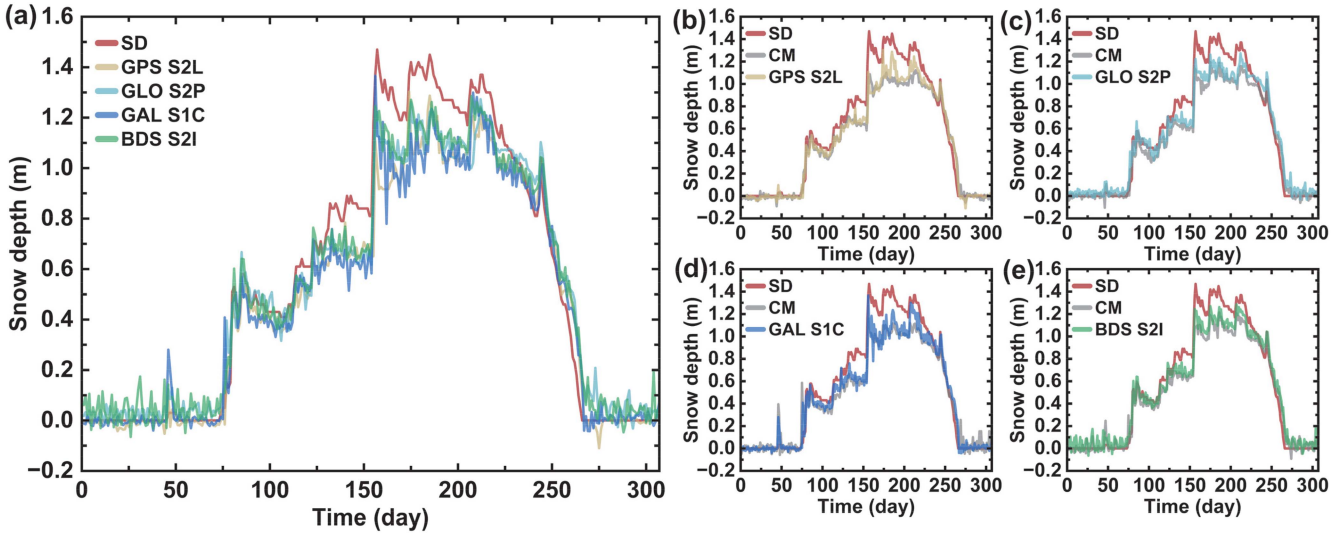


Fig. 19. Snow depth inversion results with peak ratio weighting of the optimal bands. (a) Time series of snow depth inversion values for the optimal bands. (b)–(e) Time series comparison between the inversion values and the classical method results.

TABLE IV
SNOW DEPTH INVERSION RESULTS WITH PEAK RATIO WEIGHTING OF THE OPTIMAL BANDS

| Signal | Method | ME (m) | R | RMSE (m) | Improvement rate of RMSE |
|---|---|---|---|---|---|
| GPS S2L | CM | −0.086 | 0.984 | 0.155 | – |
| | PRW | −0.062 | 0.985 | 0.135 | 12.9% |
| GLO S2P | CM | −0.079 | 0.986 | 0.144 | – |
| | PRW | −0.035 | 0.987 | 0.123 | 14.6% |
| GAL S1C | CM | −0.089 | 0.982 | 0.166 | – |
| | PRW | −0.069 | 0.983 | 0.139 | 16.3% |
| BDS S2I | CM | −0.064 | 0.987 | 0.132 | – |
| | PRW | −0.023 | 0.986 | 0.113 | 14.4% |

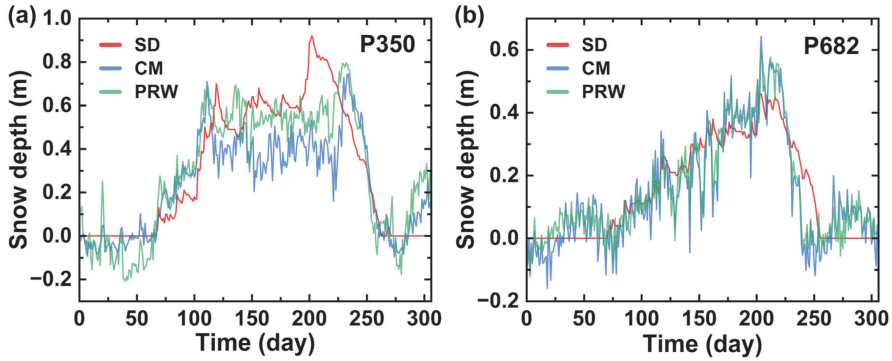


Fig. 20. Inversion results of the verification experiment. (a) Inversion results of P350 site. (b) Inversion results of P682 site.

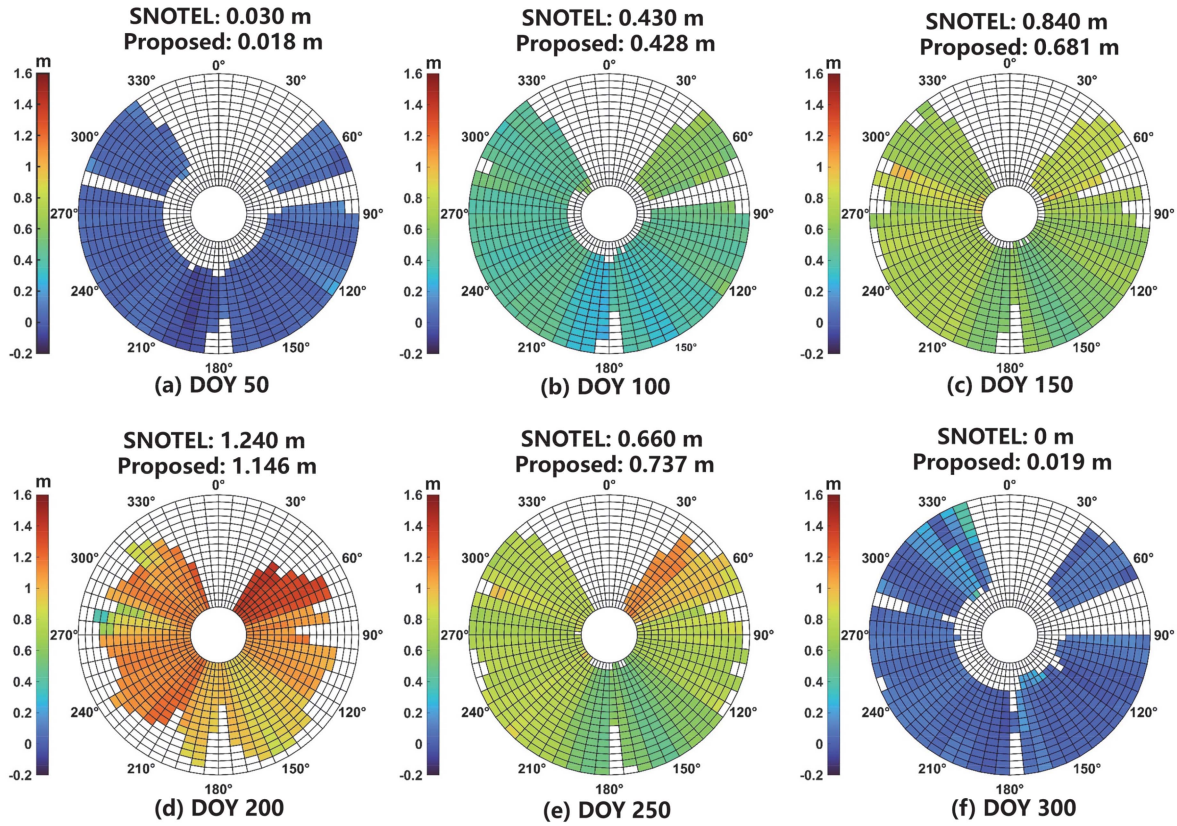


Fig. 21. Snow depth inversion map after grid-based weighted fusion. (a)–(f) Snow depth inversion results for the DOY 50, 100, 150, 200, 250, and 300.

has been significantly improved after terrain error correction and PRW. For P350 site, the $R$ value increased by 0.06, and the RMSE reduced from 0.187 to 0.150 m (an improvement of 19.8%). For P682 site, the $R$ value increased by 0.04, and the RMSE reduced from 0.094 to 0.079 m (an improvement of 16.0%).

### *F. Multi-GNSS Snow Depth Inversion With High Spatiotemporal Resolution Based on Gridding Method*

*1) Multi-GNSS Snow Depth Inversion Using the Grid Method:* After obtaining high-precision single-system snow depth inversion results through terrain error correction and PRW algorithms, it remains essential to comprehensively utilize multisystem satellite data to enhance the temporal and spatial resolution of GNSS-IR snow depth inversion. Therefore, we introduced a grid-based multi-GNSS data weighted fusion algorithm. This method involves calculating the median elevation and azimuth angles for each reflected arc segment, and using these to determine the Fresnel reflection zones' positions. The process utilizes a polar coordinate grid system centered on the site to delineate effective reflection zones and identify the positions of arc segments within them. Snow depth values are then calculated from these segments and weighted according to their position within the grid, improving the accuracy of snow

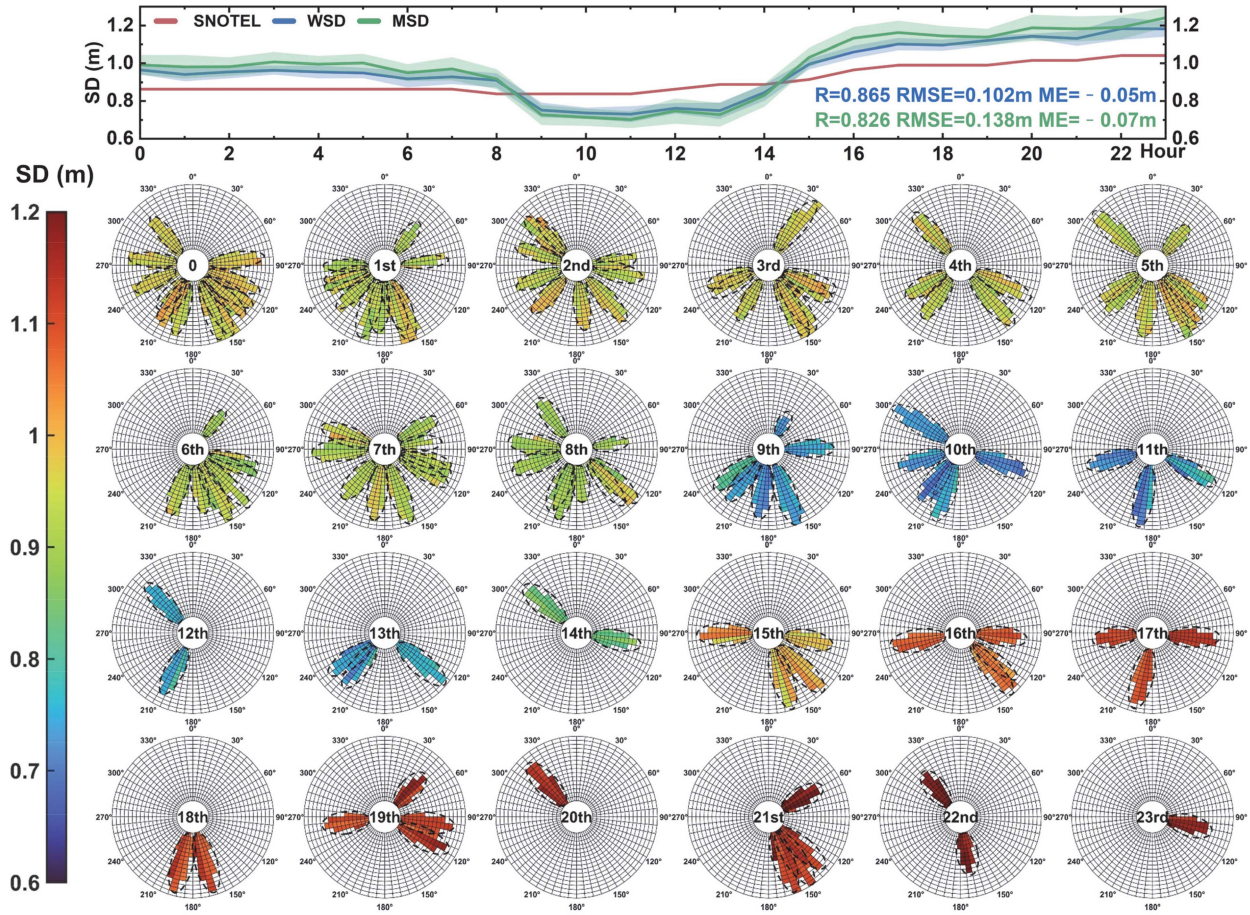


Fig. 22. Hourly snow depth inversion values of the DOY 243.

TABLE V
INVERSION RESULTS OF P350 AND P682 SITES

| Site | Method | R | RMSE (m) | Improvement rate of RMSE |
|---|---|---|---|---|
| P350 | CM | 0.801 | 0.187 | – |
| | PRW | 0.861 | 0.150 | 19.80% |
| P682 | CM | 0.844 | 0.094 | – |
| | PRW | 0.881 | 0.079 | 16.00% |

depth estimations. This grid-based, multisystem fusion approach allows for the aggregation of snow depth measurements, yielding a more accurate daily snow depth value by averaging across all grid points. We selected the optimal band data from each system for multi-GNSS snow depth inversion fusion. It is worth noting that usually, under different stations, affected by many factors such as local environment, weather, geographical location, topography, and human activities, the best band for snow depth inversion of each system is different, which needs to be analyzed by specific stations. Fig. 21 shows the snow depth inversion map after grid-based weighted fusion. The image displays the snow depth changes from 50th day to 300th day. The color transition, from blue—green—orange—red—green—blue, clearly reflects the process of snow accumulation from shallow to deep and then from deep to shallow over a snow season. Simultaneously, the grid-based weighted fusion method can effectively show the differences in snow depth in different regions around the site, enhancing the spatial resolution of snow depth inversion.

*2) Hourly Snow Depth Inversion for a Single Day:* To validate the potential of the method introduced in this article for high temporal and spatial resolution snow depth inversion, we used both the equal weight averaging method and the weighted fusion method based on gridding to inverse the hourly snow depth value of DOY 243, as shown in Fig. 22. The results indicate that based on the GNSS signal processing method discussed earlier, both methods achieved reliable hourly snow depth results. The equal weight averaging method yielded a correlation of 0.826 and an RMSE of 0.138 m. The gridding method performed even better, with an improvement in correlation by 4.72%, a decrease in RMSE by 26.09%, and a ME reduction by 28.57%, reaching values of 0.865, 0.102 m, and –0.05 m, respectively. However, when the number of available trajectories is limited, the standard deviation of the inversion results is relatively large.

*3) Hourly Snow Depth Inversion for Long Time Series:* Furthermore, we applied the methods in this paper to long time series high resolution snow depth inversion, and inversed the hourly snow depth for the whole 307-day snow season from

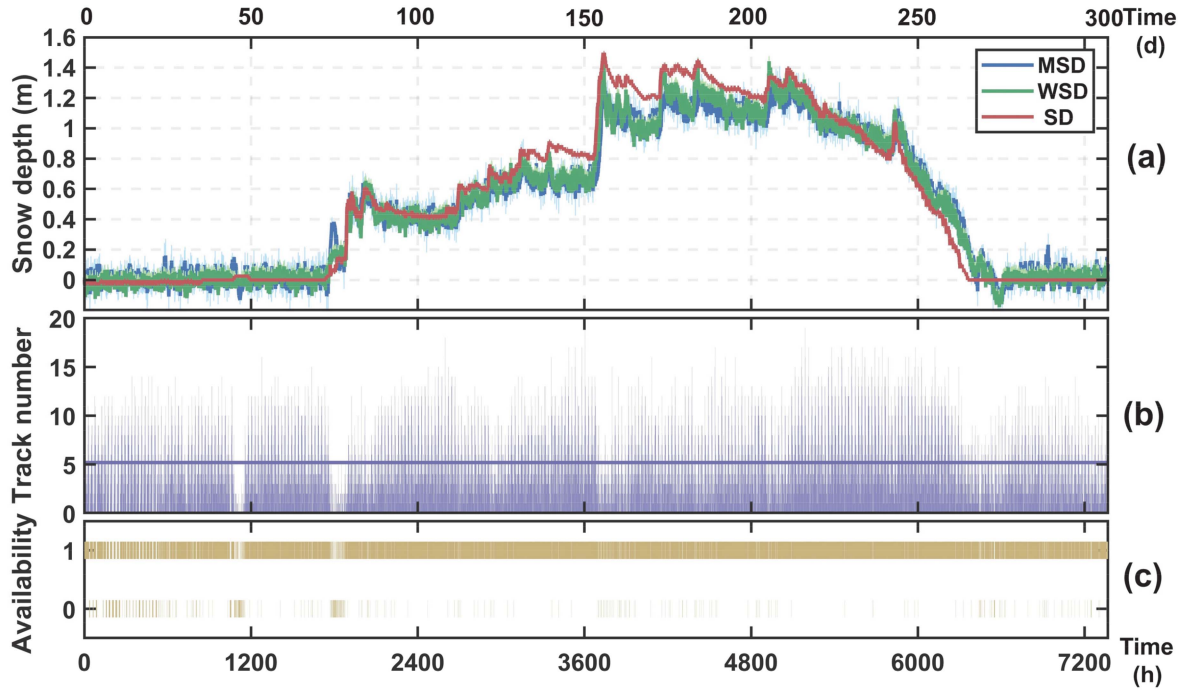


Fig. 23. Hourly snow depth inversion values for the entire snow season. (a) Snow depth inversion results. (b) Number of available trajectories per hour. (c) Availability of hourly results for the entire period. MSD represents the equal weight averaging method. WSD denotes the weighted fusion method.

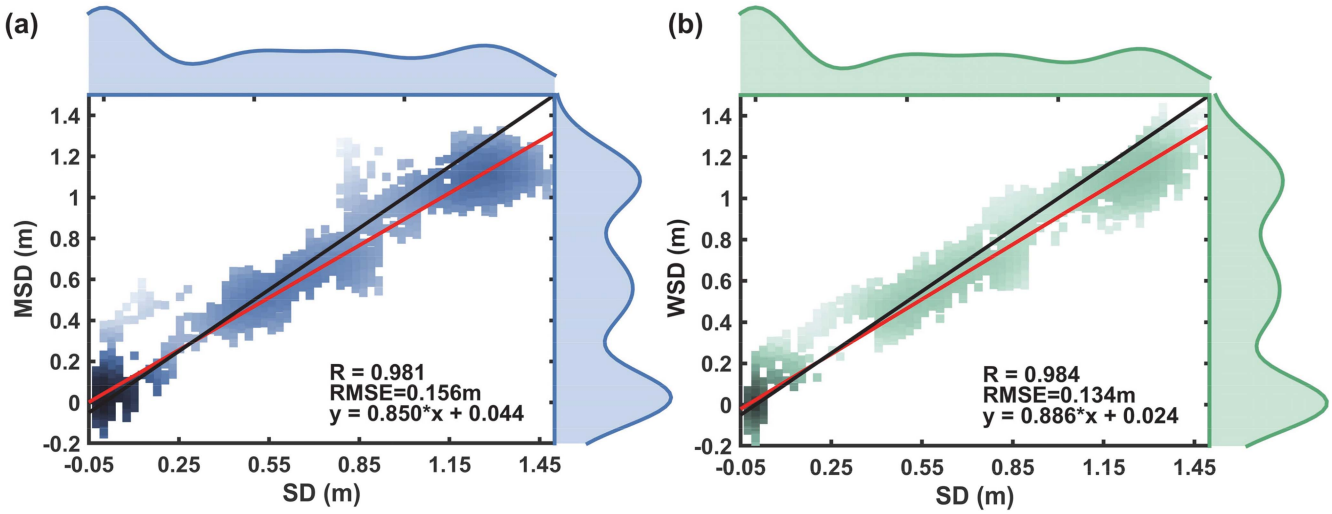


Fig. 24. Hourly snow depth inversion results for the entire snow season. (a) Scatter plots of the equal weight averaging method results against the SNOTEL references. (b) Scatter plots of the weighted fusion method results against the SNOTEL references.

DOY 193 of 2020 to DOY 180 of 2021 at the P351 site, as shown in Figs. 23 and 21. Fig. 23(a) presents the snow depth inversion results and errors for the entire snow season, with deep blue lines representing the results of the equal weight averaging method and light blue vertical lines indicating its error bars, while the green lines represent the results of the weighted fusion method based on gridding. Fig. 23(b) shows the number of available trajectories per hour, peaking at 19 trajectories in an hour and averaging five trajectories per hour. Fig. 23(c) indicates the availability of hourly results for the entire period, with 0 and 1 respectively representing the absence and presence of inversion results. The experiments demonstrate that both methods can meet the requirements for long-term high temporal and spatial resolution snow depth monitoring. Notably, whether considering snow depth inversion values or the errors, the weighted fusion inversion method achieved superior results. Although the available trajectories vary over time, an average of 5.19 trajectories is available per hour, and the coverage rate of hourly inversion results reaches 94.44% of the entire observation period. From Fig. 24, we can observe that the inversion results of both the equal weight fusion method and the weighted fusion method have a strong correlation with the reference values, which to some

extent demonstrates the effectiveness of the method introduced in this article for long-duration, high-resolution snow depth monitoring. However, the equal weight fusion method shows significant deviations in snow depths between 0–0.2 m and 0.8–1.0 m, whereas the results of the weighted fusion method are more stable. Additionally, the RMSE of the two methods has increased, with the equal weight fusion method yielding an RMSE of 0.156 m, which is 16.42% higher than the 0.134 m of the weighted fusion method.

*4) Hourly Snow Depth Inversion for Long Time Series:* Furthermore, we applied the methods in this paper to long time series high resolution snow depth inversion, and inversed the hourly snow depth for the whole 307-day snow season from DOY 193 of 2020 to DOY 180 of 2021 at the P351 site, as shown in Figs. 23 and 21. Fig. 23(a) presents the snow depth inversion results and errors for the entire snow season, with deep blue lines representing the results of the equal weight averaging method and light blue vertical lines indicating its error bars, while the green lines represent the results of the weighted fusion method based on gridding. Fig. 23(b) shows the number of available trajectories per hour, peaking at 19 trajectories in an hour and averaging five trajectories per hour. Fig. 23(c) indicates the availability of hourly results for the entire period, with 0 and 1, respectively, representing the absence and presence of inversion results. The experiments demonstrate that both methods can meet the requirements for long-term high temporal and spatial resolution snow depth monitoring. Notably, whether considering snow depth inversion values or the errors, the weighted fusion inversion method achieved superior results. Although the available trajectories vary over time, an average of 5.19 trajectories is available per hour, and the coverage rate of hourly inversion results reaches 94.44% of the entire observation period. From Fig. 24, we can observe that the inversion results of both the equal weight fusion method and the weighted fusion method have a strong correlation with the reference values, which to some extent demonstrates the effectiveness of the method introduced in this article for long-duration, high-resolution snow depth monitoring. However, the equal weight fusion method shows significant deviations in snow depths between 0–0.2 m and 0.8–1.0 m, whereas the results of the weighted fusion method are more stable. Additionally, the RMSE of the two methods has increased, with the equal weight fusion method yielding an RMSE of 0.156 m, which is 16.42% higher than the 0.134 m of the weighted fusion method.

## V. Conclusion

This study aimed to develop a method for monitoring snow depth with high precision and spatiotemporal resolution, addressing critical gaps in current methodologies. The PRW method ingeniously integrates three established strategies, repurposing each for novel objectives, thereby enhancing snow depth inversion accuracy by accounting for both terrain factors and multi-GNSS signal interactions at fine spatial scales. Unlike existing studies that primarily focus on one or two techniques, our approach leverages the combined strengths of these strategies to address the challenge of spatiotemporal matching between multi-GNSS signal trajectories and complex terrain. This holistic approach not only overcomes the limitations imposed by anisotropic terrain errors but also capitalizes on the dynamic nature of multi-GNSS signals, ensuring accurate, high-resolution monitoring across varied site locations. Initially, we analyzed the spatiotemporal availability of GNSS signals through trajectory clustering, which informed the selection of optimal inversion bands for each system. Subsequent correction of terrain errors, utilizing high-accuracy DEMs, laid the groundwork for effective spatiotemporal matching. By partitioning the study area into grids conforming to the desired resolution (limited by the DEM's resolution), applying peak ratio weighting within each grid, and fusing results from different systems based on spatial relationships between grid centroids and reflection zones, we achieved a novel solution for hourly snow depths high-resolution, high-accuracy continuous monitoring. Three sites with complete snow season GNSS data were used to validate the method in this article, leading to the following conclusions:

1) Proper signal processing techniques, such as CEEMD, can effectively mitigate the impact of GNSS signal quality, enhance data utilization, and improve inversion accuracy.
2) Terrain error correction significantly improves snow depth inversion accuracy. For the GPS, GLO, GAL, and BDS signals, the $R$ values for snow depth inversion are comparable to conventional methods. However, the RMSE decreased by 0.014, 0.012, 0.018, and 0.010 m, respectively, resulting in improvement rates of 9.0%, 8.3%, 10.8%, and 7.6%. ME also decreased by 11.63%, 49.4%, 4.50%, and 40.6%, respectively.
3) The peak ratio weighting algorithm further improves snow depth inversion accuracy compared to the terrain error correction algorithm. RMSE decreased by 4.3%, 6.8%, 6.1%, and 7.4%, respectively compared to conventional methods, representing reductions of 12.9%, 14.6%, 16.3%, and 14.4%. Moreover, snow depth inversion algorithms based on terrain error correction and peak ratio weighting maintain $R$ values similar to conventional methods, but ME decreased by 27.9%, 55.7%, 22.5%, and 64.1%, respectively.
4) The grid-based method, which weights based on reflection zone positioning, effectively integrates multi-GNSS data, achieving high-precision hourly snow depth inversions. In a single-day experiment, compared to equal-weight fusion, the $R$ improved by 4.72%, RMSE decreased by 26.09%, and the average error decreased by 28.57%, reaching values of 0.865, 0.102 m, and –0.05 m, respectively. Over the entire snow season, the weighted fusion method achieved an RMSE of 0.134 m, a 14.10% reduction from the equal-weight fusion's 0.156 m. The hourly monitoring results covered 94.44% with an average of 5.19 available trajectories.

## VI. Discussion

In summary, this article established a high-accuracy multi-GNSS snow depth inversion method that accounts for the challenge of spatiotemporal matching between multi-GNSS signal

trajectories and complex terrain, employing variable resolutions, and applied them to long time series snow depth inversion monitoring, which provides a reference for GNSS-IR snow depth inversion research. Here is a discussion on the selectivity and scalability of the solution proposed in this article in terms of spatiotemporal resolution and observational accuracy under different monitoring requirements. In this article, we divided the effective reflection area into high-resolution uniform grids of 5 m $\times$ 15°, and most of the effective reflection zones are able to cover these grids. However, by sacrificing some spatiotemporal resolution to divide the monitoring area into irregular detection zones and using GNSS signals with relatively fixed revisit trajectories for snow depth monitoring, mapping the reflection zones onto inclined surfaces can further enhance monitoring accuracy. If the spatiotemporal resolution requirements are appropriately lowered, introducing the robust estimation strategies from [21], [44] into the data fusion of single-system multifrequency signals holds great promise for further improving data utilization and the robustness of the inversion results. Furthermore, since GNSS-IR technology fundamentally involves monitoring surface parameters by estimating the frequency, amplitude, and phase of the reflected signals, the high spatiotemporal resolution solution proposed in this article can also be applicable to other areas. These include precision agriculture, where it provides high-resolution, accurate soil moisture monitoring and vegetation growth state monitoring; and disaster monitoring, where, after correcting for terrain impacts, it can capture soil moisture on landslide-prone surfaces and evaluate the risks of geological disasters. Future studies will focus on the evolution of snow conditions and the influence of underlying vegetation and soil conditions on snow depth monitoring.

## ACKNOWLEDGMENT

The authors acknowledge the EarthScope Plate Boundary Observatory operated by UNAVCO and the PBO H2O research group (http://xenon.colorado.edu/portal/) for providing the GNSS data. The SNOTEL data shown in this article were retrieved from http://www.wcc.nrcs.usda.gov/. The authors also thank these organizations for making the data available for scientific research.

## REFERENCES

[1] M. Troin, A. Poulin, M. Baraer, and F. Brissette, "Comparing snow models under current and future climates: Uncertainties and implications for hydrological impact studies," *J. Hydrol.*, vol. 540, pp. 588–602, Sep. 2016, doi: 10.1016/j.jhydrol.2016.06.055.

[2] L. R. Mudryk, P. J. Kushner, C. Derksen, and C. Thackeray, "Snow cover response to temperature in observational and climate model ensembles," *Geophys. Res. Lett.*, vol. 44, no. 2, pp. 919–926, Jan. 2017, doi: 10.1002/2016GL071789.

[3] M. A. Tomaszewska, L. H. Nguyen, and G. M. Henebry, "Land surface phenology in the highland pastures of montane Central Asia: Interactions with snow cover seasonality and terrain characteristics," *Remote Sens. Environ.*, vol. 240, Apr. 2020, Art. no. 111675, doi: 10.1016/j.rse.2020.111675.

[4] J. Dong, J. P. Walker, and P. R. Houser, "Factors affecting remotely sensed snow water equivalent uncertainty," *Remote Sens. Environ.*, vol. 97, no. 1, pp. 68–82, Jul. 2005, doi: 10.1016/j.rse.2005.04.010.

[5] J. L. Foster et al., "Quantifying the uncertainty in passive microwave snow water equivalent observations," *Remote Sens. Environ.*, vol. 94, no. 2, pp. 187–203, Jan. 2005, doi: 10.1016/j.rse.2004.09.012.

[6] J. Li, D. Yang, F. Wang, and X. Hong, "A new algorithm for measuring vegetation growth using GNSS interferometric reflectometry," *IEEE J. Sel. Topics Appl. Earth Observ. Remote Sens.*, vol. 16, pp. 1033–1041, Dec. 2023, doi: 10.1109/JSTARS.2022.3230090.

[7] M. Martin-Neira, M. Caparrini, J. Font-Rossello, S. Lannelongue, and C. S. Vallmitjana, "The PARIS concept: An experimental demonstration of sea surface altimetry using GPS reflected signals," *IEEE Trans. Geosci. Remote Sens.*, vol. 39, no. 1, pp. 142–150, Jan. 2001, doi: 10.1109/36.898676.

[8] K. M. Larson, E. D. Gutmann, V. U. Zavorotny, J. J. Braun, M. W. Williams, and F. G. Nievinski, "Can we measure snow depth with GPS receivers?," *Geophys. Res. Lett.*, vol. 36, no. 17, Sep. 2009, doi: 10.1029/2009GL039430.

[9] K. M. Larson and F. G. Nievinski, "GPS snow sensing: Results from the EarthScope plate boundary observatory," *GPS Solutions*, vol. 17, no. 1, pp. 41–52, Jan. 2013, doi: 10.1007/s10291-012-0259-7.

[10] J. L. McCreight, E. E. Small, and K. M. Larson, "Snow depth, density, and SWE estimates derived from GPS reflection data: Validation in the Western U. S.," *Water Resour. Res.*, vol. 50, no. 8, pp. 6892–6909, Aug. 2014, doi: 10.1002/2014WR015561.

[11] F. G. Nievinski and K. M. Larson, "An open source GPS multipath simulator in Matlab/Octave," *GPS Solutions*, vol. 18, no. 3, pp. 473–481, Jul. 2014, doi: 10.1007/s10291-014-0370-z.

[12] F. G. Nievinski and K. M. Larson, "Forward modeling of GPS multipath for near-surface reflectometry and positioning applications," *GPS Solutions*, vol. 18, no. 2, pp. 309–322, Apr. 2014, doi: 10.1007/s10291-013-0331-y.

[13] F. G. Nievinski and K. M. Larson, "Inverse modeling of GPS multipath for snow depth estimation—Part I: Formulation and simulations," *IEEE Geosci. Remote Sens. Lett.*, vol. 52, no. 10, pp. 6555–6563, Oct. 2014, doi: 10.1109/TGRS.2013.2297681.

[14] K. M. Larson and E. E. Small, "Estimation of snow depth using L1 GPS signal-to-noise ratio data," *IEEE J. Sel. Topics Appl. Earth Observ. Remote Sens.*, vol. 9, no. 10, pp. 4802–4808, Oct. 2016, doi: 10.1109/JSTARS.2015.2508673.

[15] S. Jin, X. Qian, and H. Kutoglu, "Snow depth variations estimated from GPS-reflectometry: A case study in alaska from L2P SNR data," *Remote Sens.*, vol. 8, no. 1, Jan. 2016, Art. no. 63, doi: 10.3390/rs8010063.

[16] S. Tabibi, F. G. Nievinski, T. van Dam, and J. F. G. Monico, "Assessment of modernized GPS L5 SNR for ground-based multipath reflectometry applications," *Adv. Space Res.*, vol. 55, no. 4, pp. 1104–1116, Feb. 2015, doi: 10.1016/j.asr.2014.11.019.

[17] X. Qian and S. Jin, "Estimation of snow depth from GLONASS SNR and phase-based multipath reflectometry," *IEEE J. Sel. Topics Appl. Earth Observ. Remote Sens.*, vol. 9, no. 10, pp. 4817–4823, Oct. 2016, doi: 10.1109/JSTARS.2016.2560763.

[18] S. Tabibi, F. Geremia-Nievinski, and T. van Dam, "Statistical comparison and combination of GPS, GLONASS, and multi-GNSS multipath reflectometry applied to snow depth retrieval," *IEEE Trans. Geosci. Remote Sens.*, vol. 55, no. 7, pp. 3773–3785, Jul. 2017, doi: 10.1109/TGRS.2017.2679899.

[19] K. Yu, Y. Li, T. Jin, X. Chang, Q. Wang, and J. Li, "GNSS-R-based snow water equivalent estimation with empirical modeling and enhanced SNR-based snow depth estimation," *Remote Sens.*, vol. 12, no. 23, Jan. 2020, Art. no. 3905, doi: 10.3390/rs12233905.

[20] J. An et al., "Snow depth variations in svalbard derived from GNSS interferometric reflectometry," *Remote Sens.*, vol. 12, no. 20, Jan. 2020, Art. no. 3352, doi: 10.3390/rs12203352.

[21] X. Wang, S. Zhang, L. Wang, X. He, and Q. Zhang, "Analysis and combination of multi-GNSS snow depth retrievals in multipath reflectometry," *GPS Solutions*, vol. 24, no. 3, May 2020, Art. no. 77, doi: 10.1007/s10291-020-00990-3.

[22] W. Zhou, Y. Liu, L. Huang, B. Ji, L. Liu, and S. Bian, "Multi-constellation GNSS interferometric reflectometry for the correction of long-term snow height retrieval on sloping topography," *GPS Solutions*, vol. 26, no. 4, Sep. 2022, Art. no. 140, doi: 10.1007/s10291-022-01333-0.

[23] Z. Li, P. Chen, N. Zheng, and H. Liu, "Accuracy analysis of GNSS-IR snow depth inversion algorithms," *Adv. Space Res.*, vol. 67, no. 4, pp. 1317–1332, Feb. 2021, doi: 10.1016/j.asr.2020.11.021.

[24] K. Boniface, J. J. Braun, J. L. McCreight, and F. G. Nievinski, "Comparison of snow data assimilation system with GPS reflectometry snow depth in the Western United States," *Hydrological Processes*, vol. 29, no. 10, pp. 2425–2437, May 2015, doi: 10.1002/hyp.10346.

[25] S. Vey, A. Güntner, J. Wickert, T. Blume, H. Thoss, and M. Ramatschi, "Monitoring snow depth by GNSS reflectometry in built-up areas: A case study for Wettzell, Germany," *IEEE J. Sel. Topics Appl. Earth Observ. Remote Sens.*, vol. 9, no. 10, pp. 4809–4816, Oct. 2016, doi: 10.1109/JSTARS.2016.2516041.
[26] S. Zhang, X. Wang, and Q. Zhang, "Avoiding errors attributable to topography in GPS-IR snow depth retrievals," *Adv. Space Res.*, vol. 59, no. 6, pp. 1663–1669, Mar. 2017, doi: 10.1016/j.asr.2016.12.031.
[27] Z. Zhang, F. Guo, and X. Zhang, "Triple-frequency multi-GNSS reflectometry snow depth retrieval by using clustering and normalization algorithm to compensate terrain variation," *GPS Solutions*, vol. 24, no. 2, Mar. 2020, Art. no. 52, doi: 10.1007/s10291-020-0966-4.
[28] W. Wan et al., "Toward terrain effects on GNSS interferometric reflectometry snow depth retrievals: Geometries, modeling, and applications," *IEEE Trans. Geosci. Remote Sens.*, vol. 60, 2022, Art. no. 4415514, doi: 10.1109/TGRS.2022.3215817.
[29] J. Zhang, S. Liu, H. Liang, W. Wan, Z. Guo, and B. Liu, "Using GNSS-IR snow depth estimation to monitor the 2022 early february snowstorm over Southern China," *Remote Sens.*, vol. 14, no. 18, Jan. 2022, Art. no. 4530, doi: 10.3390/rs14184530.
[30] N. Zheng, H. Chai, L. Chen, X. Feng, and M. Xiang, "Improvement of snow depth inversion derived from terrain tilt correction and multi-GNSS measurements using the helmert variance component estimation," *IEEE Trans. Geosci. Remote Sens.*, vol. 61, Apr. 2023, Art. no. 5800713, doi: 10.1109/TGRS.2023.3265508.
[31] X. Wang and X. He, "Evaluation of multisignal and multiorbit multipath reflectometry of BeiDou navigation satellite system," *IEEE Trans. Geosci. Remote Sens. Lett.*, vol. 20, Oct. 2023, Art. no. 1503305, doi: 10.1109/LGRS.2023.3319011.
[32] W. Zhou et al., "Coastal high-temporal sea-surface altimetry using the posterior error estimations of ionosphere-free PPP and information fusion for multi-GNSS retrievals," *Remote Sens.*, vol. 14, Nov. 2022, Art. no. 5599, doi: 10.3390/rs14215599.
[33] N. Zheng, H. Chai, L. Chen, Y. Ma, and X. Tian, "Snow depth retrieval by using robust estimation algorithm to perform multi-SNR and multi-system fusion in GNSS-IR," *Adv. Space Res.*, vol. 71, no. 3, pp. 1525–1542, Feb. 2023, doi: 10.1016/j.asr.2022.10.014.
[34] C. C. Chew, E. E. Small, K. M. Larson, and V. U. Zavorotny, "Effects of near-surface soil moisture on GPS SNR data: Development of a retrieval algorithm for soil moisture," *IEEE Trans. Geosci. Remote Sens.*, vol. 52, no. 1, pp. 537–543, Jan. 2014, doi: 10.1109/TGRS.2013.2242332.
[35] R. Ding, N. Zheng, H. Zhang, H. Zhang, F. Lang, and W. Ban, "A study of GNSS-IR soil moisture inversion algorithms integrating robust estimation with machine learning," *Sustainability*, vol. 15, no. 8, Apr. 2023, Art. no. 6919, doi: 10.3390/su15086919.
[36] Y. Liang et al., "GNSS-IR multisatellite combination for soil moisture retrieval based on wavelet analysis considering detection and repair of abnormal phases," *Measurement*, vol. 203, Nov. 2022, Art. no. 111881, doi: 10.1016/j.measurement.2022.111881.
[37] X. Wang, X. He, J. Shi, S. Chen, and Z. Niu, "Estimating sea level, wind direction, significant wave height, and wave peak period using a geodetic GNSS receiver," *Remote Sens. Environ.*, vol. 279, Sep. 2022, Art. no. 113135, doi: 10.1016/j.rse.2022.113135.
[38] K. Dragomiretskiy and D. Zosso, "Variational mode decomposition," *IEEE Trans. Signal Process.*, vol. 62, no. 3, pp. 531–544, Feb. 2014, doi: 10.1109/TSP.2013.2288675.
[39] Y. Hu, X. Yuan, W. Liu, J. Wickert, and Z. Jiang, "GNSS-R snow depth inversion based on variational mode decomposition with multi-GNSS constellations," *IEEE Geosci. Remote Sens. Lett.*, vol. 60, 2022, Art. no. 2005512, doi: 10.1109/TGRS.2022.3182987.
[40] Y. Hu, X. Yuan, W. Liu, Q. Hu, J. Wickert, and Z. Jiang, "Snow depth estimation from GNSS SNR data using variational mode decomposition," *GPS Solutions*, vol. 27, no. 1, Dec. 2022, Art. no. 33, doi: 10.1007/s10291-022-01371-8.
[41] J.-R. Yeh, J.-S. Shieh, and N. E. Huang, "Complementary ensemble empirical mode decomposition: A novel noise enhanced data analysis method," *Adv. Adapt. Data Anal.*, vol. 02, no. 2, pp. 135–156, Apr. 2010, doi: 10.1142/S1793536910000422.
[42] X. Wang, X. He, R. Xiao, M. Song, and D. Jia, "Millimeter to centimeter scale precision water-level monitoring using GNSS reflectometry: Application to the South-to-North water diversion project, China," *Remote Sens. Environ.*, vol. 265, Nov. 2021, Art. no. 112645, doi: 10.1016/j.rse.2021.112645.
[43] W. Zhou, L. Liu, L. Huang, Y. Yao, J. Chen, and S. Li, "A new GPS SNR-based combination approach for land surface snow depth monitoring," *Sci. Rep.*, vol. 9, Mar. 2019, Art. no. 3814, doi: 10.1038/s41598-019-40456-2.
[44] X. Wang, X. He, and Q. Zhang, "Evaluation and combination of quad-constellation multi-GNSS multipath reflectometry applied to sea level retrieval," *Remote Sens. Environ.*, vol. 231, Sep. 2019, Art. no. 111229, doi: 10.1016/j.rse.2019.111229.

**Rui Ding** received the B.Sc. degree in surveying and mapping engineering and the M.S. degree in surveying and mapping from the East China University of Technology, Nanchang, China, in 2017 and 2020, respectively. He is currently working toward the Ph.D. degree in geodesy and surveying engineering in the School of Environment Science and Spatial Informatics, China University of Mining and Technology, Xuzhou, China.

His research interests include GNSS-R and signal processing.

**Nanshan Zheng** received the Ph.D. degree in urban environment from Kyoto University, Kyoto, Japan, in 2009.

He is currently a Professor with the School of Environment and Spatial Informatics, China University of Mining and Technology, Xuzhou, China. He has authored or coauthored more than 60 peer-reviewed journal or conference articles. His current research interests include GNSS-R, signal processing, and remote sensing of environment and disaster.

**Georges Stienne** received the M.Sc. degree in image and signal processing and the Ph.D. degree in signal processing from the University of the Littoral Opal Coast (ULCO), Calais, France, in 2010 and 2013 respectively.

After holding a postdoctoral position with Purdue University, West Lafayette, IN, USA, he has been an Associate Professor with ULCO since 2015. His works deal with the statistical estimation of the parameters of multifrequencies global navigation satellite systems (GNSS) signals, with application to GNSS positioning and GNSS-Reflectometry (GNSS-R), a bistatic remote sensing technique for Earth observation. His main research interests include GNSS-R in the domains of soil moisture estimation, sea state retrieval and altimetry measurements, for which he develops filtering, data fusion, change point detection and regression techniques, with a specific focus on angular data such as the phase of GNSS signals.

**Jiaxing He** received the B.Sc. degree in surveying and mapping engineering from the Chengdu University of Technology, Chengdu, China, in 2018, and the M.S. degree in geodesy and engineering surveying from the School of Environment Science and Spatial Informatics, China University of Mining and Technology, Xuzhou, China, in 2023.

His research interests include GNSS-R and machine learning.

**Hengyi Zhang** received the B.Sc. degree in surveying and mapping engineering from the Guilin University of Technology, Guilin, China, in 2020, and the M.S. degree in surveying and mapping engineering from the School of Environment Science and Spatial Informatics, China University of Mining and Technology, Xuzhou, China, in 2023.

His research interests include GNSS-R snow depth inversion.

**Xuexi Liu** received the Ph.D. degree with distinction in geodesy and engineering surveying from the School of Geodesy and Geomatics, Wuhan University, Wuhan, China, in 2022.

He is currently an Associate Professor with the China University of Mining and Technology, Xuzhou, China. His current research interests include multi-GNSS precise point positioning and biases estimation, satellite orbit determination, and clock offset estimation.